DYNAMICS OF RESONANCES AND EQUILIBRIA OF LOW EARTH OBJECTS

ALESSANDRA CELLETTI AND CĂTĂLIN GALEŞ

ABSTRACT. The nearby space surrounding the Earth is densely populated by artificial satellites and instruments, whose orbits are distributed within the Low-Earth-Orbit region (LEO), ranging between 90 and 2000 km of altitude. As a consequence of collisions and fragmentations, many space debris of different sizes are left in the LEO region. Given the threat raised by the possible damages which a collision of debris can provoke with operational or manned satellites, the study of their dynamics is nowadays mandatory. This work is focused on the existence of equilibria and the dynamics of resonances in LEO. We base our results on a simplified model which includes the geopotential and the atmospheric drag. Using such model, we make a qualitative study of the resonances and the equilibrium positions, including their location and stability. The dissipative effect due to the atmosphere provokes a tidal decay, but we give examples of different behaviors, precisely a straightforward passage through the resonance or rather a temporary capture. We also investigate the effect of the solar cycle which is responsible of fluctuations of the atmospheric density and we analyze the influence of Sun and Moon on LEO objects.

1. INTRODUCTION

The region of space above the Earth is plenty of satellites with different purposes: Earth's observation including remote sensing and meteorological satellites, the International Space Station (ISS), the Space Shuttle, the Hubble Space Telescope. All of them are moving in the so-called Low-Earth-Orbit (hereafter LEO) region, which ranges between 90 and 2000 km of altitude above the Earth's surface. Satellites in LEO are characterized by a high orbital speed and might possess different inclinations, even reaching very high values as in the case of polar orbits, among which Sun-synchronous satellites can be found. Satellites can be permanently located in LEO or they can just cross that region as in the case of *highly elliptical orbits,* characterized by a large eccentricity that leads to big excursions, possibly across the LEO region.

Being easy to reach, LEOs are convenient for building space platforms and installing instruments. The disadvantages of placing a satellite in LEO are due to the closeness

to the Earth and to the air drag. Indeed, the Earth's oblateness has a key role and must be accurately modeled by including a suitable number of coefficients of the series expansion of the geopotential (compare with Formiga & Vilhena del Moraes (2011); Liu & Alford (1980)). On the other hand, the presence of the atmosphere provokes an air drag, which acts as a dissipative force (see, e.g., Bezdek & Vokrouhlický (2004); Chao (2005); Delhaise (1991); Gaias et al. (2015)). Its strength depends on the altitude, since the air density decreases with the distance from the Earth's surface and it may change due to the Solar activity (for density models we refer to Jacchia (1971); Hedin (1986, 1991); ISO 27852 (2010)). The drag provokes a tidal decay of the satellite on time scales which depend on the altitude of the satellite, hence on the density of the atmosphere. Beside the gravitational attraction of the Earth, the air drag and the Earth's oblateness, a comprehensive model includes also the influence of the Moon, the attraction of the Sun and the Solar radiation pressure (see Kaula (1962); Celletti & Galeş (2016); Celletti et al. (2016); Ely & Howell (1997)). We refer to Alessi et al. (2016); Celletti & Galeş (2014, 2015a,b); Celletti et al. (2017b); Daquin et al. (2016); Gedeon (1969); Gkolias (2016); Lemaître et al. (2009); Rosengren & Scheeres (2013); Rosengren et al. (2014); Valk et al. (2009) (and references therein) for a description of the dynamics at distances from the Earth higher than LEO.

The large number of satellites in LEO unavoidably provokes a huge amount of space junk, as a consequence of collisions between satellites or due to the fact that the satellites' remnants are left there at the end of their operational life. The spatial density of the debris has a peak around $800\ km$, as a consequence of the collisions between the satellites Iridium and Cosmos in 2009 and the breakup of Fengyun-1C in 2007. Collisions with space debris might provoke dramatic events, due to the high speed during the impact. The U.S. Space Surveillance Network tracks in LEO about $400\,000$ debris between $1\ cm$ and $10\ cm$, and $14\,000$ debris larger than $10\ cm$. Objects of $1\ cm$ size might damage a spacecraft and even break the ISS shields; debris of $10\ cm$ size might provoke a fragmentation of a satellite.

More than half of the total amount of space debris is in LEO, thus increasing the interest for the dynamical behavior of objects in this region, which is the main goal of the present work. The knowledge of the dynamics of the space debris can considerably contribute to the development of mitigation measures, most notably through the design

of suitable post-mission disposal orbits (see, e.g., Deienno et al. (2016)). Among the possible mitigation strategies, one can provoke a re-entry of the debris in the lower atmosphere or rather a transfer to an orbit with a different lifetime. It is therefore of paramount importance to know whether an object is located in a regular, resonant or chaotic region, as well as to know how much time will spend in such regions. This paper aims to contribute to give an answer to these question.

This work extends the research performed in Celletti & Galeş (2014, 2015a), where analytical and numerical methods, mostly adopting Hamiltonian formalism, have been used to study the dynamics of objects within resonances located at large distances from the Earth (the so-called geostationary and GPS regions at distances, respectively, equal to $42\,164\ km$ and $26\,560\ km$). We also mention Ely & Howell (1997); Formiga & Vilhena del Moraes (2011); Lemaître et al. (2009); Valk et al. (2009) for accurate modeling and analytical studies of space debris dynamics. With respect to Celletti & Galeş (2014, 2015a), the current work presents the novelty that, dealing with LEO, the model becomes more complicated, due to the effect of the geopotential, being the Earth very close, and moreover the dynamics is dissipative because of the air drag.

The dynamics is described through a set of equations of motion which include the geopotential, the atmospheric drag and the contribution of Sun and Moon. In particular, we study four specific resonances located in LEO at different altitudes; such resonances are due to a commensurability between the orbital period of the debris and the period of rotation of the Earth. The geopotential is expanded in spherical harmonics, although only a limited number of coefficients is taken into account, precisely those which contribute to shape the dynamics, being the dominant terms in a specific region of orbital parameters. The atmospheric drag is modeled through a set of equations which are first averaged with respect to the mean anomaly and then translated in terms of the Delaunay actions. A qualitative study of the resonances is based on the construction of a *toy model*, which provides a sound analytical support to the numerical investigation of the problem. We are thus able to draw conclusions about the role of the dissipation, the location and stability character of the equilibria, the occurrence of temporary capture into a resonance or rather a straight passage through it. Once the results for the toy model are obtained, we pass to investigate a problem which includes the change of the local density of the atmosphere due to the effect of the solar cycle and the gravitational influence given by Sun and Moon. The study leads to interesting results, which can be used in concrete cases to make a thorough analysis of the dynamics of space debris and

even to design possible disposal orbits, or rather to provide practical solutions for control and maintenance of LEO satellites. Due to dissipative effects, frequent maneuvers are required to keep the orbital altitude. Our study reveals strong evidence that there exists equilibrium points in LEO that might be used in practice by parking operational satellites in their close vicinity, thus reducing the cost of maintenance.

This paper is organized as follows. In Section 2 we provide the equations of motion in Delaunay action-angle coordinates derived from a Hamiltonian including the Keplerian part and the effect of the oblateness of the Earth. The geopotential is expanded in Section 3 using a classical development in terms of the spherical harmonic coefficients. A model for the atmospheric drag is provided in Section 4. Resonances, equilibria and their stability are analyzed in Section 5, while the effect of the the solar cycle and lunisolar perturbations are studied in Section 6.

2. EQUATIONS OF MOTION

We consider a small body, say S, located in the LEO region around the Earth. We study its perturbed motion, taking into account the oblateness of the Earth, the rotation of our planet and the atmospheric drag. To introduce the equations of motion, we use the action–angle Delaunay variables, denoted as $(L, G, H, M, \omega, \Omega)$, which are related to the orbital elements $(a, e, i, M, \omega, \Omega)$ by the expressions

$$L = \sqrt{\mu_E a}\,, \qquad G = L\sqrt{1 - e^2}\,, \qquad H = G \cos i\,, \qquad (2.1)$$

where a is the semimajor axis, e the eccentricity, i the inclination, M the mean anomaly, ω the argument of perigee, Ω the longitude of the ascending node and $\mu_E = \mathcal{G} m_E$ with $\mathcal{G}$ the gravitational constant and m_E the mass of the Earth.

We denote by $\mathcal{H}$ the geopotential Hamiltonian (see Celletti & Galeş (2014)), which can be written as

$$\mathcal{H}(L, G, H, M, \omega, \Omega, \theta) = -\frac{\mu_E^2}{2L^2} + \mathcal{H}_{earth}(L, G, H, M, \omega, \Omega, \theta)\,, \qquad (2.2)$$

where θ is the sidereal time, $-\frac{\mu_E^2}{2L^2}$ is the Keplerian part and $\mathcal{H}_{earth}$ represents the perturbing function (for which an explicit approximate expression is given in Section 3).

We denote by F_L, F_G, F_H the components of the dissipative effects due to the atmospheric drag, whose explicit expressions are given in Section 4. Then, the dynamical

equations of motion are given by

$$\dot{M} = \frac{\partial \mathcal{H}}{\partial L}, \qquad \dot{\omega} = \frac{\partial \mathcal{H}}{\partial G}, \qquad \dot{\Omega} = \frac{\partial \mathcal{H}}{\partial H},$$
$$\dot{L} = -\frac{\partial \mathcal{H}}{\partial M} + F_L, \qquad \dot{G} = -\frac{\partial \mathcal{H}}{\partial \omega} + F_G, \qquad \dot{H} = -\frac{\partial \mathcal{H}}{\partial \Omega} + F_H. \tag{2.3}$$

3. The geopotential Hamiltonian

Following Kaula (1966), we expand $\mathcal{H}_{earth}$ as

$$\mathcal{H}_{earth} = -\frac{\mu_E}{a} \sum_{n=2}^{\infty} \sum_{m=0}^{n} \left(\frac{R_E}{a}\right)^n \sum_{p=0}^{n} \overline{F}_{nmp}(i) \sum_{q=-\infty}^{\infty} G_{npq}(e) \, \overline{S}_{nmpq}(M, \omega, \Omega, \theta), \tag{3.1}$$

where R_E is the Earth's radius, $\overline{F}_{nmp}$ the normalized inclination function defined as

$$\overline{F}_{nmp} = \sqrt{\frac{(2 - \delta_{0n})(2n + 1)(n - m)!}{(n + m)!}} \, F_{nmp},$$

where δ_{0n} is the Kronecker function, the inclination and eccentricity functions F_{nmp}, G_{npq} are computed by well–known recursive formulae (see, e.g., Kaula (1966); Chao (2005); Celletti & Galeş (2014)), while $\overline{S}_{nmpq}$ is expressed as

$$\overline{S}_{nmpq} = \left[\begin{array}{c} \overline{C}_{nm} \\ -\overline{S}_{nm} \end{array} \right]_{n-m \ odd}^{n-m \ even} \cos \Psi_{nmpq} + \left[\begin{array}{c} \overline{S}_{nm} \\ \overline{C}_{nm} \end{array} \right]_{n-m \ odd}^{n-m \ even} \sin \Psi_{nmpq}, \tag{3.2}$$

where $\overline{C}_{nm}$ and $\overline{S}_{nm}$ are, respectively, the cosine and sine normalized coefficients of the spherical harmonics potential terms (see Table 1 for concrete values) and

$$\Psi_{nmpq} = (n - 2p)\omega + (n - 2p + q)M + m(\Omega - \theta). \tag{3.3}$$

The normalized coefficients $\overline{C}_{nm}$ and $\overline{S}_{nm}$ are related to the geopotential coefficients C_{nm} and S_{nm} through the expressions (see Kaula (1966); Montenbruck & Gill (2000)):

$$\left(\begin{array}{c} \overline{S}_{nm} \\ \overline{C}_{nm} \end{array} \right) = \sqrt{\frac{(n + m)!}{(2 - \delta_{0n})(2n + 1)(n - m)!}} \left(\begin{array}{c} S_{nm} \\ C_{nm} \end{array} \right).$$

As we shall see later, we consider resonant motions which involve the rate of variations of the mean anomaly and the sidereal angle through a linear combination with integer coefficients (see Definition 1 below). We shall be interested in specific resonances, which will correspond to linear combinations involving the index m with $m \geq 11$ (see Table 4 below).

Since we deal with harmonic terms with large order (precisely $m \geq 11$), we use the normalized coefficients, which have the advantage of being more uniform in magnitude than the unnormalized coefficients. In fact, the size of the normalized coefficients is

expressed approximately by the empirical Kaula's rule (see Kaula (1966)): $\overline{C}_{nm}$, $\overline{S}_{nm} \simeq 10^{-5}/n^2$, and therefore they decay less rapidly with n. This allows us to avoid some computational complications which might appear when working with very small numbers, such as C_{nm}, S_{nm} for large n, or very big numbers, which are involved in the computation of F_{nmp}.

As common in geodesy, we introduce also the quantities $\overline{J}_{nm}$ defined by

$$\overline{J}_{nm} = \sqrt{\overline{C}_{nm}^2 + \overline{S}_{nm}^2} \quad \text{if } m \neq 0 , \qquad \overline{J}_{n0} \equiv \overline{J}_n = -\overline{C}_{n0}$$

and the quantities λ_{nm} defined through the relations

$$\overline{C}_{nm} = -\overline{J}_{nm} \cos(m\lambda_{nm}) , \qquad \overline{S}_{nm} = -\overline{J}_{nm} \sin(m\lambda_{nm}) . \tag{3.4}$$

The coefficients $\overline{J}_{nm}$ in units of 10^{-6} as well as the values of λ_{nm}, involved in the study of the resonances, are given in Table 1; they are computed according to the Earth's gravitational model EGM2008 (EGM (2008)).

n	m	$\overline{J}_{nm}$	λ_{nm}	n	m	$\overline{J}_{nm}$	λ_{nm}	n	m	$\overline{J}_{nm}$	λ_{nm}
2	0	484.1651	$0°$	15	11	0.0186	$-7°\!.82$	19	11	0.0193	$19°\!.31$
3	0	-0.9572	$0°$	15	12	0.036	$-2°\!.14$	19	12	0.0098	$-6°\!.29$
4	0	-0.54	$0°$	15	13	0.0287	$0°\!.70$	19	13	0.0295	$5°\!.78$
5	0	-0.0687	$0°$	15	14	0.0249	$7°\!.29$	19	14	0.0137	$4°\!.98$
6	0	0.15	$0°$	16	11	0.0194	$15°\!.50$	20	11	0.024	$11°\!.55$
7	0	-0.0905	$0°$	16	12	0.0207	$16°\!.58$	20	12	0.0193	$-5°\!.86$
11	11	0.0836	$11°\!.23$	16	13	0.0138	$14°\!.18$	20	13	0.0282	$14°\!.91$
12	11	0.013	$13°\!.70$	16	14	0.0432	$4°\!.53$	20	14	0.0184	$9°\!.19$
12	12	0.0114	$6°\!.47$	17	11	0.0195	$-3°\!.15$	21	12	0.0151	$-6°\!.44$
13	11	0.0448	$0°\!.56$	17	12	0.0353	$17°\!.96$	21	13	0.0239	$-2°\!.75$
13	12	0.0933	$-5°\!.87$	17	13	0.026	$17°\!.74$	21	14	0.0216	$14°\!.28$
13	13	0.0916	$-3°\!.70$	17	14	0.0184	$-2°\!.79$	22	13	0.026	$-3°\!.74$
14	11	0.0421	$10°\!.17$	18	11	0.0072	$-1°\!.56$	22	14	0.0137	$15°\!.53$
14	12	0.0323	$8°\!.77$	18	12	0.034	$2°\!.43$	23	14	0.0071	$12°\!.01$
14	13	0.0555	$18°\!.04$	18	13	0.0355	$6°\!.14$				
14	14	0.0521	$0°\!.38$	18	14	0.0153	$4°\!.08$				

TABLE 1. The values of $\overline{J}_{nm}$ (in units of 10^{-6}) and the quantities λ_{nm} computed from EGM (2008).

3.1. **Approximation of the Hamiltonian.** The expansion of the disturbing function $\mathcal{H}_{earth}$ in (3.1) contains an infinite number of trigonometric terms, but the long term

variation of the orbital elements is mainly governed by the secular and resonant terms. Moreover, for the gravitational resonances located in the GEO and MEO regions, we pointed out in Celletti & Galeş (2014, 2015b,a) that just some of these terms are really relevant for the dynamics.

In the present work, we perform the study of the effects of the *gravitational resonances* (also called *tesseral* resonances, see Gedeon (1969); Ely & Howell (1997)), within the LEO region. The precise definition of resonance is given as follows.

Definition 1. *A tesseral (or gravitational) resonance of order $j : k$ with j, $k \in \mathbb{Z}\backslash\{0\}$ occurs when the orbital period of the debris and the rotational period of the Earth are commensurable of order $j : k$. In terms of the orbital elements, a $j : k$ gravitational resonance occurs if*

$$k\,\dot{M} - j\,\dot{\theta} = 0 \ , \qquad j, k \in \mathbb{N} \ .$$

Following Celletti & Galeş (2014, 2015b,a), we approximate $\mathcal{H}_{earth}$ by

$$\mathcal{H}_{earth} = \mathcal{H}_{earth}^{sec} + \mathcal{H}_{earth}^{res} + \mathcal{H}_{earth}^{nonres} \cong \sum_{n=2}^{N}\sum_{m=0}^{n}\sum_{p=0}^{n}\sum_{q=-\infty}^{\infty} \mathcal{T}_{nmpq} \ ,$$

where $\mathcal{H}_{earth}^{sec}$, $\mathcal{H}_{earth}^{res}$, $\mathcal{H}_{earth}^{nonres}$ denote, respectively, the secular, resonant and non–resonant contributions to the Earth's potential, the approximation index $N \in \mathbb{Z}_{+}$ will be given later, while the coefficients $\mathcal{T}_{nmpq}$ are defined by:

$$\mathcal{T}_{nmpq} = -\frac{\mu_E R_E^n}{a^{n+1}}\,\overline{F}_{nmp}(i)G_{npq}(e)\overline{S}_{nmpq}(M,\omega,\Omega,\theta) \ . \tag{3.5}$$

In the following we describe the secular part of the expansion (3.1) by computing the average over the fast angles, say $\mathcal{H}_{earth}^{sec}$, and the resonant part associated to a given $j : k$ tesseral resonance, say $\mathcal{H}_{earth}^{resj:k}$.

Since the value of the oblateness coefficient $\overline{J}_2 = \overline{J}_{20}$ is much larger than the value of any other zonal coefficient (see Table 1), we consider the same secular part for all resonances; the explicit expression of the secular part will be given in Section 3.1.1.

Concerning the resonant part, say $\mathcal{H}_{earth}^{res\,j:k}$, it is essential to retain a minimum number of significant terms in practical computations. The criteria for selecting these terms are described in Section 3.2.

3.1.1. *The secular part of $\mathcal{H}_{earth}$.* With reference to the expression for $\overline{S}_{nmpq}$ given in (3.2)-(3.3), the secular terms correspond to $m = 0$ and $n - 2p + q = 0$. From Table 1, it is clear that $\overline{J}_2 \gg \overline{J}_n$ for all $n \in \mathbb{N}$, $n > 2$. Therefore, in the secular part the most important harmonic is $\overline{J}_2$. Moreover, from Table 1 it follows that $|\overline{J}_3|$ and $|\overline{J}_4|$ are larger

than $|\overline{J}_n|$, $n > 4$. Since we are interested in orbits having small eccentricities, for our purposes it is enough to consider just a few harmonic terms in the expansion of the secular part. In practical computations, for all resonances considered in the forthcoming sections, we approximate the secular part with the following expression, computed e.g. in Celletti & Galeş (2014):

$$
\begin{aligned}
\mathcal{H}^{sec}_{earth} &= \frac{\sqrt{5}\mu_E R_E^2 \overline{J}_2}{a^3}\left(\frac{3}{4}\sin^2 i - \frac{1}{2}\right)(1-e^2)^{-3/2} \\
&+ \frac{2\sqrt{7}\mu_E R_E^3 \overline{J}_3}{a^4}\left(\frac{15}{16}\sin^3 i - \frac{3}{4}\sin i\right)e(1-e^2)^{-5/2}\sin\omega \\
&+ \frac{3\mu_E R_E^4 \overline{J}_4}{a^5}\left[\left(-\frac{35}{32}\sin^4 i + \frac{15}{16}\sin^2 i\right)\frac{3e^2}{2}(1-e^2)^{-7/2}\cos(2\omega)\right. \\
&+ \left.\left(\frac{105}{64}\sin^4 i - \frac{15}{8}\sin^2 i + \frac{3}{8}\right)(1+\frac{3e^2}{2})(1-e^2)^{-7/2}\right] .
\end{aligned}
\tag{3.6}
$$

It is important to stress that the numerical results, obtained by taking into account the above approximation of the secular part, may be analytically explained by considering only the influence of $\overline{J}_2$; this will lead to consider a *toy model*, which well describes the dynamics, as it will be explained in Section 5. The results based on the toy model will allow to draw conclusions about the importance of $\overline{J}_2$ with respect to the other harmonics.

Clearly, in view of (2.1), $\mathcal{H}^{sec}_{earth}$ can be written as a function of L, G, H and ω.

3.1.2. *The resonant part of $\mathcal{H}_{earth}$.* From (3.2)-(3.3) we see that the terms associated to a resonance of order $j:k$ correspond to $j(n-2p+q) = k\,m$. We consider the resonant part corresponding to the following resonances located in the close vicinity of the Earth: 11:1, 12:1, 13:1 and 14:1. As we will show in Table 4 below, the resonances 11:1, 12:1, 13:1, 14:1 range from an altitude equal to $2\,146.61\ km$ down to an altitude equal to 880.55 km.

Hence, we consider $k = 1$ and, within all possible combinations, the solution for which $j = m$ and $n - 2p + q = 1$ is relevant for our purposes.

Since the majority of infinitesimal bodies of the LEO region moves on almost circular orbits, we focus our analysis on small eccentricities with $e \in [0, 0.02]$. For such orbits, just some harmonic resonant terms are significant for the dynamics; their selection will be made by using an analytical argument. In fact, we will see that the resonant part can be approximated with a large degree of accuracy by the sum of some terms, whose

formal expression is:

$$\mathcal{H}^{res\,m:1}_{earth} = \begin{cases} \sum_{\alpha=0}^{N} A^m_\alpha(L,G,H)\cos(\sigma_{m1} - m\,\lambda_{m+2\alpha,m}), & \text{if } m = 11 \text{ or } m = 13, \\ \sum_{\alpha=0}^{N} A^m_\alpha(L,G,H)\sin(\sigma_{m1} - m\,\lambda_{m+2\alpha+1,m}), & \text{if } m = 12 \text{ or } m = 14, \end{cases}$$
(3.7)

where the resonant angle is defined by

$$\sigma_{m1} = M - m\theta + \omega + m\Omega,$$
(3.8)

N is a natural number sufficiently large so that the approximation of the resonant part includes all harmonic terms with high magnitude (in this work we take $N = 4$), $A^m_\alpha(L,G,H)$ might be computed by using (3.1) and (2.1), once $\overline{F}_{nmp}$ and G_{npq} are known, while the values of the constants λ_{nm} are given in Table 1.

In a more compact notation, $\mathcal{H}^{res\,m:1}_{earth}$ is written as:

$$\mathcal{H}^{res\,m:1}_{earth} = \mathcal{A}^{(m)}_0(L,G,H)\cos(\sigma_{m1} - \varphi^{(m)}_0(L,G,H)),$$
(3.9)

where $\mathcal{A}^{(m)}_0(L,G,H)$ and $\varphi^{(m)}_0(L,G,H)$ are defined through the relations

$$\mathcal{A}^{(m)}_0(L,G,H)\cos\varphi^{(m)}_0(L,G,H) = \sum_{\alpha=0}^{N} A^m_\alpha(L,G,H)\cos(m\lambda_{m+2\alpha,m}),$$

$$\mathcal{A}^{(m)}_0(L,G,H)\sin\varphi^{(m)}_0(L,G,H) = \sum_{\alpha=0}^{N} A^m_\alpha(L,G,H)\sin(m\lambda_{m+2\alpha,m}) \qquad \text{if } m = 11 \text{ or } m = 13$$
(3.10)

and

$$\mathcal{A}^{(m)}_0(L,G,H)\cos\varphi^{(m)}_0(L,G,H) = -\sum_{\alpha=0}^{N} A^m_\alpha(L,G,H)\sin(m\lambda_{m+2\alpha+1,m}),$$

$$\mathcal{A}^{(m)}_0(L,G,H)\sin\varphi^{(m)}_0(L,G,H) = \sum_{\alpha=0}^{N} A^m_\alpha(L,G,H)\cos(m\lambda_{m+2\alpha+1,m}) \qquad \text{if } m = 12 \text{ or } m = 14.$$
(3.11)

To provide the analytical explanation of how the relevant harmonic terms can be selected, we need two essential comments on the index q labeling the term $\mathcal{T}_{nmpq}$ (see (3.5)). First, we notice that the coefficients $G_{npq}(e)$ decay as powers of the eccentricity, precisely $G_{npq}(e) = \mathcal{O}(e^{|q|})$ (see Kaula (1966); Celletti & Galeş (2014)). Henceforth, the term $\mathcal{T}_{nmpq}$ is of order $|q|$ in the eccentricity. On the other hand, in view of (3.2), (3.3), (3.4) and (3.8), it follows that the argument of the resonant term $\mathcal{T}_{nmpq}$ has the form $\sigma_{m1} - q\omega + const$. Therefore, we conclude that the resonant harmonic terms can be grouped into terms of the same order in the eccentricity and having the same argument (modulo a constant).

Let us denote by $\mathcal{M}_q^m$ the set of the resonant terms associated to the resonance $m:1$ and having the same index q, namely

$$\mathcal{M}_q^m \equiv \{\mathcal{T}_{nmpq}: \ n - 2p + q = 1 \ , \ n \in \mathbb{N} \ , \ p \in \mathbb{N} \ , \ n \geq m \ , \ p \leq n\} \ . \tag{3.12}$$

The sets $\mathcal{M}_q^m$ with $q = -1, 0, 1$ and for the resonances 11:1, 12:1, 13:1, 14:1 are given in Table 2. The introduction of the set $\mathcal{M}_q^m$ is motivated by the fact that, from a dynamical point of view, the terms belonging to $\mathcal{M}_q^m$ combine to give rise to a single resonant island at the same altitude. Indeed, as it was pointed out in Celletti & Galeş (2014) and Celletti & Galeş (2015a), each resonance splits into a multiplet of resonances; the exact location of the resonance for each component of the multiplet is obtained as the solution of the relation $\dot{\sigma}_{m1} - q\dot{\omega} = 0$. However, since the elements of the set $\mathcal{M}_q^m$ have the same argument $\sigma_{m1} - q\omega$ (modulo a constant), a single resonant island is obtained when n and p vary, even if $\mathcal{M}_q^m$ includes terms which are all different from each other. Using (3.1), (3.2), (3.3), (3.5), (3.8), we have the following result.

Lemma 2. *The sum of the terms of the set $\mathcal{M}_q^m$ in (3.12) can be written formally as*

$$\sum_{\mathcal{T} \in \mathcal{M}_q^m} \mathcal{T} = \mathcal{A}_q^{(m)}(L, G, H) \cos(\sigma_{m1} - q\omega - \varphi_q^{(m)}(L, G, H)) \ ,$$

where $\mathcal{A}_q^{(m)}(L, G, H)$ and $\varphi_q^{(m)}(L, G, H)$ can be explicitly computed for each set $\mathcal{M}_q^m$, once its elements are known.

Without loss of generality, we assume that $\mathcal{A}_q^{(m)}(L, G, H)$ is non-negative for every L, G, H, possibly shifting the argument of the trigonometric function.

3.2. **The most relevant terms of the Hamiltonian.** Our next task is to retain those sets $\mathcal{M}_q^m$ which are important for the dynamics, as well as to keep only the most relevant elements of each selected set. Since our analysis involves small eccentricities, one expects that $\mathcal{M}_0^m$ will play the most important role, while the influence of the other sets, precisely $\mathcal{M}_{-1}^m$, $\mathcal{M}_1^m$, will be weaker. Concerning the elements of the set $\mathcal{M}_q^m$, it is important to stress that the coefficients of degree n decay as $(R_E/a)^n$, so the role of the harmonic terms with higher degree becomes increasingly less influent. However, since we are considering resonances which are very close to the Earth, the quantity $(R_E/a)^n$ decays slowly for increasingly higher values of n. In conclusion, to get a reliable model, the set $\mathcal{M}_q^m$ should contain as many harmonic terms as possible. However, due to computational limitations, in this paper the maximum number of elements of $\mathcal{M}_q^m$ is 5, which is a

$m:1$	$\mathcal{M}_q^m$	terms
11:1	$\mathcal{M}_0^{11}$	$\mathcal{T}_{11\,11\,5\,0}, \mathcal{T}_{13\,11\,6\,0}, \mathcal{T}_{15\,11\,7\,0}, \mathcal{T}_{17\,11\,8\,0}, \mathcal{T}_{19\,11\,9\,0}$
	$\mathcal{M}_{-1}^{11}$	$\mathcal{T}_{12\,11\,5\,-1}, \mathcal{T}_{14\,11\,6\,-1}, \mathcal{T}_{16\,11\,7\,-1}, \mathcal{T}_{18\,11\,8\,-1}, \mathcal{T}_{20\,11\,9\,-1}$
	$\mathcal{M}_1^{11}$	$\mathcal{T}_{12\,11\,6\,1}, \mathcal{T}_{14\,11\,7\,1}, \mathcal{T}_{16\,11\,8\,1}, \mathcal{T}_{18\,11\,9\,1}, \mathcal{T}_{20\,11\,10\,1}$
12:1	$\mathcal{M}_0^{12}$	$\mathcal{T}_{13\,12\,6\,0}, \mathcal{T}_{15\,12\,7\,0}, \mathcal{T}_{17\,12\,8\,0}, \mathcal{T}_{19\,12\,9\,0}, \mathcal{T}_{21\,12\,10\,0}$
	$\mathcal{M}_{-1}^{12}$	$\mathcal{T}_{12\,12\,5\,-1}, \mathcal{T}_{14\,12\,6\,-1}, \mathcal{T}_{16\,12\,7\,-1}, \mathcal{T}_{18\,12\,8\,-1}, \mathcal{T}_{20\,12\,9\,-1}$
	$\mathcal{M}_1^{12}$	$\mathcal{T}_{12\,12\,6\,1}, \mathcal{T}_{14\,12\,7\,1}, \mathcal{T}_{16\,12\,8\,1}, \mathcal{T}_{18\,12\,9\,1}, \mathcal{T}_{20\,12\,10\,1}$
13:1	$\mathcal{M}_0^{13}$	$\mathcal{T}_{13\,13\,6\,0}, \mathcal{T}_{15\,13\,7\,0}, \mathcal{T}_{17\,13\,8\,0}, \mathcal{T}_{19\,13\,9\,0}, \mathcal{T}_{21\,13\,10\,0}$
	$\mathcal{M}_{-1}^{13}$	$\mathcal{T}_{14\,13\,6\,-1}, \mathcal{T}_{16\,13\,7\,-1}, \mathcal{T}_{18\,13\,8\,-1}, \mathcal{T}_{20\,13\,9\,-1}, \mathcal{T}_{22\,13\,10\,-1}$
	$\mathcal{M}_1^{13}$	$\mathcal{T}_{14\,13\,7\,1}, \mathcal{T}_{16\,13\,8\,1}, \mathcal{T}_{18\,13\,9\,1}, \mathcal{T}_{20\,13\,10\,1}, \mathcal{T}_{22\,13\,11\,1},$
14:1	$\mathcal{M}_0^{14}$	$\mathcal{T}_{15\,14\,7\,0}, \mathcal{T}_{17\,14\,8\,0}, \mathcal{T}_{19\,14\,9\,0}, \mathcal{T}_{21\,14\,10\,0}, \mathcal{T}_{23\,14\,11\,0}$
	$\mathcal{M}_{-1}^{14}$	$\mathcal{T}_{14\,14\,6\,-1}, \mathcal{T}_{16\,14\,7\,-1}, \mathcal{T}_{18\,14\,8\,-1}, \mathcal{T}_{20\,14\,9\,-1}, \mathcal{T}_{22\,14\,10\,-1}$
	$\mathcal{M}_1^{14}$	$\mathcal{T}_{14\,14\,7\,1}, \mathcal{T}_{16\,14\,8\,1}, \mathcal{T}_{18\,14\,9\,1}, \mathcal{T}_{20\,14\,10\,1}, \mathcal{T}_{22\,14\,11\,1},$

TABLE 2. The sets $\mathcal{M}_0^m$, $\mathcal{M}_{-1}^m$, $\mathcal{M}_1^m$ for the resonances 11:1, 12:1, 13:1, 14:1.
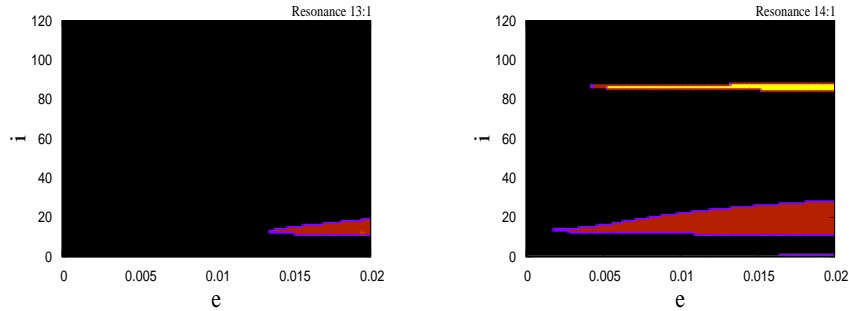

FIGURE 1. Dominant sets for the 13:1 (left) and 14:1 (right) resonances as a function of eccentricity and inclination: $\mathcal{M}_0^m$ – black, $\mathcal{M}_{-1}^m$ – brown, $\mathcal{M}_1^m$ – yellow, where $m = 13$, 14 and the sets $\mathcal{M}_0^m$, $\mathcal{M}_{-1}^m$, $\mathcal{M}_1^m$ are defined in Section 3.1.2.

good compromise between accuracy and complexity. It is meaningful to consider a larger number of coefficients when dealing with specific concrete cases.

To give an explicit example, let us take the set $\mathcal{M}_0^{11}$. Comparing the coefficient $(R_E/a)^{11}$ of the term $\mathcal{T}_{11\,11\,5\,0}$ (see (3.5) and Table 2) with the coefficient $(R_E/a)^{21}$ of $\mathcal{T}_{21\,11\,10\,0}$ (namely, the first term of $\mathcal{M}_0^{11}$ neglected in our computations), we find that for $a = 8524.75$ km (see Table 4 below) the term $\mathcal{T}_{21\,11\,10\,0}$ is 18 times smaller than $\mathcal{T}_{11\,11\,5\,0}$, thus showing that the neglected harmonic terms are smaller in magnitude than those

considered in our model. Of course, the conclusion is valid for all other sets, although with different ratios. We report in Table 2 the terms of the sets $\mathcal{M}_0^m$, $\mathcal{M}_{-1}^m$ and $\mathcal{M}_1^m$ that we are going to consider for each resonance.

Once the elements of $\mathcal{M}_q^m$ are selected, it remains to discriminate which are the most important ones. Making use of Lemma 2, we introduce the following definition, which gives a hierarchy between the sets $\mathcal{M}_q^m$.

Definition 3. *Let $\mathcal{H}_{earth}^{res\,m:1}$ be the resonant part of $\mathcal{H}_{earth}$, corresponding to the resonance $m:1$. For given values of the orbital elements (a, e, i), equivalently for given values of (L, G, H), we say that a set $\mathcal{M}_q^m$, for some $q \in \mathbb{Z}$, is dominant with respect to the other sets $\mathcal{M}_{\widetilde{q}}^m$, where $\widetilde{q} \in \mathbb{Z}$ with $\widetilde{q} \neq q$, if $\mathcal{A}_q^{(m)}(L, G, H) \geq \mathcal{A}_{\widetilde{q}}^{(m)}(L, G, H)$ for all $\widetilde{q} \in \mathbb{Z}$.*

A plot of the dominant sets according to Definition 3 for the resonances $13:1$ and $14:1$ is provided in Figure 1, within the orbital elements' intervals $e \in [0, 0.02]$ and $i \in [0^o, 120^o]$. The black, brown and yellow colors are, respectively, used to show the regions where $\mathcal{M}_0^m$, $\mathcal{M}_{-1}^m$ and $\mathcal{M}_1^m$ dominate. Similar plots are also obtained for the 11:1 and 12:1 resonances, but in these cases the regions associated to $\mathcal{M}_{-1}^m$ are very small and those related to $\mathcal{M}_1^m$ are negligible. From the analysis of Figure 1, we conclude that $\mathcal{M}_0^m$ is dominant in almost all regions of the (e, i) - plane, except for some small inclinations and for $i = 86.18^o$ in the case of the 14:1 resonance. Taking into account the fact that the amplitudes of the two resonant islands associated to $\mathcal{M}_{-1}^m$ and $\mathcal{M}_1^m$ are small (at most few hundred meters as it will be shown in Section 5), we may approximate the resonant part $\mathcal{H}_{earth}^{res\,m:1}$ by the sum of the terms of $\mathcal{M}_0^m$. Therefore, from Table 2 and collecting (3.2), (3.3), (3.4), (3.5), (3.8), it follows that $\mathcal{H}_{earth}^{res\,m:1}$ can be written in the form (3.7) (or equivalently in the form (3.9)) for a suitable integer N, which counts the number of terms generated by $\mathcal{M}_0^m$. Section 5 will confirm that the analytical model, constructed on the basis of this approximation, leads to reliable results. In fact, the numerical investigation will be performed by taking into account the effects of all three sets $\mathcal{M}_0^m$, $\mathcal{M}_{-1}^m$ and $\mathcal{M}_1^m$, but we will obtain results that can be easily explained in terms of an analytical model which includes just the influence of $\mathcal{M}_0^m$.

Since the normalized inclination functions $\overline{F}_{nmp}$ involve very long expressions (often more than half page for each function), we avoid giving the explicit forms of the terms $\mathcal{T}_{nmpq}$ and of the functions $A_\alpha^m(L, G, H)$, $\mathcal{A}_0^{(m)}(L, G, H)$ and $\varphi_0^{(m)}(L, G, H)$. The reader can compute these quantities by using the recursive formulae for the functions F_{nmp},

G_{npq} (see Kaula (1966); Celletti & Galeş (2014)) and by using the relations presented in Section 3.1.

4. Dissipative effects: the atmospheric drag

During its motion within the Earth's atmosphere, an infinitesimal object (satellite or space debris) encounters air molecules, whose change of momentum gives rise to a dissipative force oriented opposite to the motion of the body and known as atmospheric drag. The atmospheric drag force depends on the local density of the atmosphere, the velocity of the object relative to the atmosphere and the cross–sectional area in the direction of motion.

The purpose of this Section is to derive the functions F_L, F_G, F_H, characterizing the atmospheric drag perturbations in the dynamical equations (2.3). To this end, we use the following averaged equations of variation of the orbital elements (see Liu & Alford (1980); Chao (2005)):

$$
\begin{aligned}
\dot{a} &= -\frac{1}{2\pi} \int_0^{2\pi} B\,\rho\,v\,\frac{a}{1-e^2}\left[1+e^2+2e\cos f - \omega_E \cos i \sqrt{\frac{a^3(1-e^2)^3}{\mu_E}}\right]\,dM \\
&\equiv \mathcal{F}^{(a)}(a,e,i)\ , \\
\dot{e} &= -\frac{1}{2\pi} \int_0^{2\pi} B\,\rho\,v\left[e+\cos f - \frac{r^2\omega_E \cos i}{2\sqrt{\mu_E a(1-e)^2}}\Big(2(e+\cos f) - e\sin^2 f\Big)\right]\,dM \\
&\equiv \mathcal{F}^{(e)}(a,e,i)\ ,
\end{aligned}
\tag{4.1}
$$

where f is the true anomaly, ω_E (coinciding with $\dot{\theta}$) is the Earth's rotation rate, ρ the atmospheric density, B the ballistic coefficient, while the body's speed relative to the atmosphere is given by

$$
v = \sqrt{\frac{\mu_E}{a(1-e^2)}(1+e^2+2e\cos f)}\left(1 - \frac{(1-e^2)^{\frac{3}{2}}}{1+e^2+2e\cos f}\frac{\omega_E}{n^*}\cos i\right)\ ,
\tag{4.2}
$$

where n^* is the mean motion of the satellite. Notice that r, f (hence v) are functions of M. We stress that the atmospheric drag affects just $\dot{a}$ and $\dot{e}$ and not the other variables (namely, the inclination and the angle variables).

We recall that the ballistic coefficient is expressed in terms of the cross–sectional area A with respect to the relative wind and in terms of the mass m of the object through the formula $B = C_D\,A/m$, where C_D is the drag coefficient. For a debris, the coefficient B can vary by a factor 10 depending on the satellite's orientation (see Table 8-3 in Larson & Wertz (1999) for a list of estimated ballistic coefficients associated to various

Altitude h_0 (km)	Atm. scale height H_0 (km)	Minimum density (kg/m^3)	Mean density (kg/m^3)	Maximum density (kg/m^3)
700	99.3	$5.74 \cdot 10^{-15}$	$2.72 \cdot 10^{-14}$	$1.47 \cdot 10^{-13}$
800	151	$2.96 \cdot 10^{-15}$	$9.63 \cdot 10^{-15}$	$4.39 \cdot 10^{-14}$
1000	296	$1.17 \cdot 10^{-15}$	$2.78 \cdot 10^{-15}$	$8.84 \cdot 10^{-15}$
1250	408	$4.67 \cdot 10^{-16}$	$1.11 \cdot 10^{-15}$	$2.59 \cdot 10^{-15}$
1500	516	$2.30 \cdot 10^{-16}$	$5.21 \cdot 10^{-16}$	$1.22 \cdot 10^{-15}$
2000	829	–	–	–

TABLE 3. The scaling height H_0 as well as the minimum, mean and maximum densities at the reference altitude h_0, from MSIS atmospheric model (Hedin (1991), see also Larson & Wertz (1999)).

LEO satellites; note that this table provides $1/B$). Although the ballistic coefficient of a satellite slightly modifies in time, in all simulations we suppose that B is constant. This assumption is motivated by the fact that we are interested in studying the equilibrium points, and therefore in such dynamical configuration the small variation of B can be neglected in a first approximation. Moreover, in order to show the existence of the equilibrium points even for strong dissipative effects, in our simulations we shall often use large values for the ballistic coefficient, up to $2200 \, cm^2/kg$, although the value for a satellite is much smaller, typically $25 \leq B \leq 500 \, cm^2/kg$ (see ISO 27852 (2010)).

To complete the discussion of equations (4.1), let us mention that the atmospheric density can be computed from density models such as that developed by Jacchia (Jacchia (1971)), the Mass Spectrometer Incoherent Scatter - MSIS model (Hedin (1986, 1991)) and other models (see ISO 27852 (2010)). Following the dynamical density MSIS model, the local density is a function of various parameters such as the altitude of the body, the solar flux, the Earth's magnetic index, etc. (see Hedin (1986, 1991)). Of particular interest is the variation of density as effect of the solar activity, which fluctuates with an 11–year cycle.

In this work we use the numbers provided by the MSIS model. Therefore, we assume that the local density varies with the altitude above the surface, say $h = r - R_E$, with r the distance from the Earth's center, and we use the the following barometric formula:

$$\rho(h) = \rho_0 \, \exp\left(-\frac{h - h_0}{H_0}\right) , \qquad (4.3)$$

where ρ_0 is the (minimum, mean or maximum) density, estimated for (minimum, mean or maximum) solar activity at the reference altitude h_0, while H_0 is the scaling height at

h_0. Reference empirical values are given in Table 3 (see also Larson & Wertz (1999)) for a more detailed list of values and further explanations).

Although our investigation involves small eccentricities, say up to $e = 0.02$, the difference in altitude between apogee and perigee is not negligible and it amounts to about 300 km (see Table 4). In fact, comparing the altitudes reported in Tables 4 and 3, it is clear that $\rho = 0$ for the 11:1 resonance, while for the other resonances one should use the formula (4.3) with the corresponding values for ρ_0, h_0 and H_0 taken from Table 3.

$m:1$	a (km)	Altitude (km)	Perigee altitude for $e = 0.02$ (km)	Apogee altitude for $e = 0.02$ (km)
11:1	8524.75	2146.61	1976.25	2317.25
12:1	8044.32	1666.18	1505.43	1827.21
13:1	7626.31	1248.17	1095.78	1400.84
14:1	7258.69	880.55	735.52	1025.86

TABLE 4. The semimajor axis and the altitude corresponding to some resonances of order $m:1$, as well as the perigee and apogee altitudes of a resonant elliptic orbit with $e = 0.02$. The altitudes are computed by considering the reference value $R_E = 6378.14$ km for the Earth's radius.

Once the framework has been settled, we can approximate in the computations the true anomaly f (entering (4.1), (4.2)) and the altitude h (entering in (4.3)) by the following well known series (Roy (2004); Celletti (2010)):

$$f = M + 2e \sin M + \frac{5e^2}{4} \sin(2M) + O(e^3) ,$$

$$h = a(1 - e \cos f) - R_E = a\left\{1 - e \cos M + \frac{e^2}{2}\left[1 - \cos(2M)\right]\right\} - R_E + O(e^3) ,$$

(4.4)

where $O(e^3)$ denotes terms of order 3 in the eccentricity. Casting together the relations (4.1), (4.2), (4.3) and (4.4), by the algebraic manipulator Mathematica$^©$ we compute the integrals appearing in the right hand side of (4.1). In this way, we deduce that the right hand sides in the first of (4.1), thereby denoted as $\mathcal{F}^{(a)}$ and $\mathcal{F}^{(e)}$, are functions of a, e, i, while ρ_0 and B are parameters. As in Section 3.1.2 we do not provide the explicit form of $\mathcal{F}^{(a)}(a, e, i)$ and $\mathcal{F}^{(e)}(a, e, i)$, since they involve long expressions. The reader can self-compute these functions by a simple implementation of the above formulae, possibly using an algebraic manipulator. Once $\mathcal{F}^{(a)}$ and $\mathcal{F}^{(e)}$ are computed as a function

of the orbital elements, it is trivial to express them in terms of the Delaunay actions:
$\mathcal{F}^{(a)} = \mathcal{F}^{(a)}(L, G, H)$ and $\mathcal{F}^{(e)} = \mathcal{F}^{(e)}(L, G, H)$.

Since the atmospheric drag does not affect the inclination, from (2.1) we obtain

$$\dot{L} = \frac{1}{2}\sqrt{\frac{\mu_E}{a}}\,\dot{a}\,,$$

$$\dot{G} = \frac{1}{2}\sqrt{\frac{\mu_E(1-e^2)}{a}}\,\dot{a} - e\sqrt{\frac{\mu_E a}{1-e^2}}\,\dot{e}\,,$$

$$\dot{H} = \left(\frac{1}{2}\sqrt{\frac{\mu_E(1-e^2)}{a}}\,\dot{a} - e\sqrt{\frac{\mu_E a}{1-e^2}}\,\dot{e}\right)\cos i\,.$$

Using the relations $a = L^2/\mu_E$, $e = \sqrt{1 - G^2/L^2}$ and $\cos i = H/G$, we deduce that the functions F_L, F_G, F_H, characterizing the atmospheric drag perturbations in (2.3), are given by

$$F_L = \frac{\mu_E}{2L}\,\mathcal{F}^{(a)}(L, G, H)\,,$$

$$F_G = \frac{\mu_E G}{2L^2}\,\mathcal{F}^{(a)}(L, G, H) - \frac{L^2}{G}\sqrt{1 - \frac{G^2}{L^2}}\,\mathcal{F}^{(e)}(L, G, H)\,, \qquad (4.5)$$

$$F_H = \frac{H}{G}\left(\frac{\mu_E G}{2L^2}\,\mathcal{F}^{(a)}(L, G, H) - \frac{L^2}{G}\sqrt{1 - \frac{G^2}{L^2}}\,\mathcal{F}^{(e)}(L, G, H)\right)\,.$$

In conclusion, to study the main dynamical features of tesseral resonances, we have introduced (Sections 2, 3 and 4) a mathematical model characterized by the equations (2.3), where the secular part of the Hamiltonian (2.2) is given by (3.6), the resonant part of $\mathcal{H}$ is obtained as the sum of the resonant harmonic terms of Table 2, while the dissipative part is described by the functions F_L, F_G, F_H defined by (4.5). Hereafter, this model will be called the *dissipative model of LEO resonances*, or simply DMLR.

5. A QUALITATIVE STUDY OF RESONANCES

This section presents a qualitative study of the resonances. Precisely, it includes an analysis of the conservative and dissipative effects, an estimate of the amplitude of the resonances, a study related to the existence, location and stability of the equilibrium points. Some analytical results based on a toy model that will be introduced in Section 5.1 are confirmed by numerical simulations obtained by using the DMLR.

We stress that, although the degree n of the resonant terms is large ($n \geq 11$), which implies that the magnitude of these terms is small, the effects of the conservative part

can be quantified; in particular, for some inclinations the resonant regions have a width larger than one or two kilometers. Since at high altitudes the drag effect is sufficiently low, even if the solar activity reaches its maximum, for such inclinations one can show that equilibrium points exist.

5.1. **The toy model.** To give an analytical support to the numerical results that will be performed on the DMLR, we construct in parallel a simplified model, to which we refer as the *toy model,* allowing to explain the main features of the dynamics. In this model the secular part contains just the $\bar{J}_2$ term (first term of (3.6)), the resonant part is defined by (3.9) and the dissipative functions are given by (5.2) below. Following Chao (2005), for nearly circular orbits, the function $\mathcal{F}^{(a)}$ can be simplified as

$$\mathcal{F}^{(a)} = -B\rho n^* a^2 \left(1 - \frac{\omega_E}{n^*}\cos i\right)^2 , \qquad (5.1)$$

where ρ is assumed to be constant at a fixed altitude of the orbit and $n^* = \sqrt{\mu_E/a^3}$. As mentioned before, the variation of the eccentricity can be considered a small quantity; therefore, in the simplified model we take $\mathcal{F}^{(e)} = 0$. Using (2.1), (4.5) and (5.1) we get

$$F_L = -\frac{1}{2}B\rho\mu_E\left(1 - \frac{\omega_E L^3 H}{\mu_E^2 G}\right)^2 , \qquad F_G = \frac{G}{L}F_L , \qquad F_H = \frac{H}{L}F_L . \qquad (5.2)$$

In view of (2.1), (2.2), (3.6), (3.9), the conservative part of the toy model is given by

$$\mathcal{H}_{toy}^{m:1}(L, G, H, \sigma_{m1}) = -\frac{\mu_E^2}{2L^2} + \frac{\alpha}{L^3 G^3}\left(1 - 3\frac{H^2}{G^2}\right) + \mathcal{A}_0^{(m)}(L, G, H)\cos(\sigma_{m1} - \varphi_0^{(m)}(L, G, H)) , \qquad (5.3)$$

where

$$\alpha = \frac{\sqrt{5}R_E^2 \bar{J}_2 \mu_E^4}{4}$$

and σ_{m1}, $\mathcal{A}_0^{(m)}$, $\varphi_0^{(m)}$ are given by (3.8), (3.10), (3.11).

Let us now perform a canonical change of coordinates, similar to that presented in Celletti & Galeş (2014), which transforms the variables $(L, G, H, M, \omega, \Omega)$ into $(\widetilde{L}, \widetilde{G}, \widetilde{H}, \sigma_{m1}, \omega, \Omega)$, where σ_{m1} is given by (3.8), ω and Ω are kept unaltered and

$$\widetilde{L} = L , \qquad \widetilde{G} = G - L , \qquad \widetilde{H} = H - mL . \qquad (5.4)$$

In terms of the new variables, the Hamiltonian (5.3) takes the form

$$\widetilde{\mathcal{H}}_{toy}^{m:1}(\widetilde{L}, \widetilde{G}, \widetilde{H}, \sigma_{m1}) = \widetilde{h}^{(m)}(\widetilde{L}, \widetilde{G}, \widetilde{H}) + \varepsilon\widetilde{\mathcal{A}}^{(m)}(\widetilde{L}, \widetilde{G}, \widetilde{H})\cos(\sigma_{m1} - \widetilde{\varphi}^{(m)}(\widetilde{L}, \widetilde{G}, \widetilde{H})) , \quad (5.5)$$
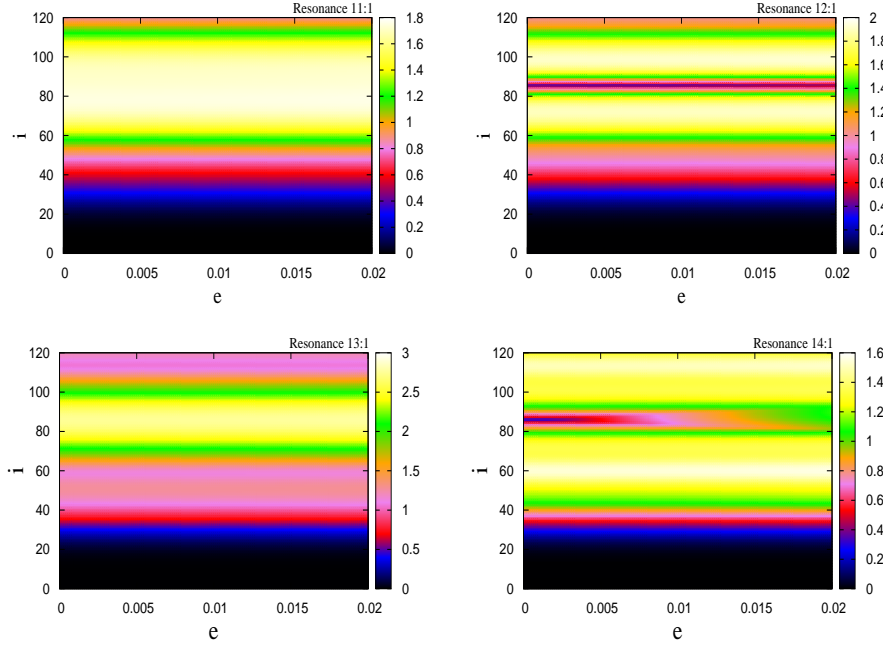
FIGURE 2. The amplitude of the resonances for different values of the
eccentricity (within 0 and 0.02 on the horizontal axis) and the inclination
(within 0° and 120° on the vertical axis); the color bar provides the
measure of the amplitude in kilometers. In order from top to bottom, left
to right: 11:1, 12:1, 13:1, 14:1.

where

$$\begin{aligned}
\widetilde{h}^{(m)}(\widetilde{L}, \widetilde{G}, \widetilde{H}) &= -\frac{\mu_E^2}{2\widetilde{L}^2} - m\widetilde{L} + \frac{\alpha}{\widetilde{L}^3(\widetilde{G}+\widetilde{L})^3}\Big(1 - 3\frac{(\widetilde{H}+m\widetilde{L})^2}{(\widetilde{G}+\widetilde{L})^2}\Big), \\
\varepsilon\widetilde{\mathcal{A}}^{(m)}(\widetilde{L}, \widetilde{G}, \widetilde{H}) &= \mathcal{A}_0^{(m)}(\widetilde{L}, \widetilde{G}+\widetilde{L}, \widetilde{H}+m\widetilde{L}), \\
\widetilde{\varphi}^{(m)}(\widetilde{L}, \widetilde{G}, \widetilde{H}) &= \varphi_0^{(m)}(\widetilde{L}, \widetilde{G}+\widetilde{L}, \widetilde{H}+m\widetilde{L})
\end{aligned}$$
(5.6)

and ε is a small coefficient introduced for convenience, so that $\widetilde{h}^{(m)}$ and $\widetilde{\mathcal{A}}^{(m)}$ have comparable sizes, when measured at the same point.

Strictly speaking, the quantity $\widetilde{\varphi}^{(m)}(\widetilde{L}, \widetilde{G}, \widetilde{H})$ depends on the variable $\widetilde{L}$ and not on $\widetilde{L}_{res}$, which is the value of $\widetilde{L}$ at the resonance. However, the numerical tests show that the error is very small, of the order of few arcseconds, if $\widetilde{\varphi}^{(m)}(\widetilde{L}, \widetilde{G}, \widetilde{H})$ is replaced by $\widetilde{\varphi}^{(m)}(\widetilde{L}_{res}, \widetilde{G}, \widetilde{H})$. Since we are interested in obtaining a reduced model, allowing to

explain the results provided by the DMLR, we take $\widetilde{\varphi}^{(m)}$ as constant in $\widetilde{L}$ and write $\widetilde{\varphi}^{(m)} = \widetilde{\varphi}^{(m)}(\widetilde{G}, \widetilde{H})$ in order to underline this aspect.

Before analyzing the dissipative part, let us study first the conservative effects. Therefore, we disregard for the moment the influence of the drag force and we focus our attention on the Hamiltonian (5.5). Since ω and Ω are cyclic variables, it results that $\widetilde{G}$ and $\widetilde{H}$ are constants, so that the dynamics is described by a pendulum type Hamiltonian. In particular, following the method described in Celletti & Galeş (2014), the width of the resonances can be easily computed for the pendulum-like model. We refer to Celletti & Galeş (2015a) for the formulae necessary to compute the amplitudes of the islands associated to (5.3). Figure 2 provides the amplitudes of the 11:1, 12:1, 13:1 and 14:1 resonances as the eccentricity varies between 0 and 0.02, while the inclination ranges between 0° and 120°. The color bar indicates the size of the amplitude in kilometers.

Figure 2 shows that for inclinations less than 30° the amplitude is small, at most $350\,m$, while for larger inclinations, the amplitude could reach about two (or three for the 13:1 resonance) kilometers. Having in mind these results, we can anticipate what happens when the dissipative effects are taken into account for the 12:1, 13:1, 14:1 resonances: we expect the equilibrium points to persist for those inclinations which lead (in the conservative case) to large amplitudes, even if the ballistic coefficient is high. On the contrary, for small inclinations – since the amplitude is small – one has the opposite situation: the magnitude of the drag force is large in comparison with the resonant part and, therefore, we anticipate that the equilibrium points do not exist. These statements are proved analytically in Sections 5.2, 5.3.

For the moment, let us go back to the equations of motion and discuss about the dissipative part. Collecting (2.3), (5.2), (5.4) and (5.5), we obtain:

$$\dot{\sigma}_{m1} = \frac{\partial \widetilde{\mathcal{H}}_{toy}^{m:1}}{\partial \widetilde{L}}\,, \qquad \dot{\omega} = \frac{\partial \widetilde{\mathcal{H}}_{toy}^{m:1}}{\partial \widetilde{G}}\,, \qquad \dot{\Omega} = \frac{\partial \widetilde{\mathcal{H}}_{toy}^{m:1}}{\partial \widetilde{H}}\,,$$

$$\dot{\widetilde{L}} = -\frac{\partial \widetilde{\mathcal{H}}_{toy}^{m:1}}{\partial \sigma_{m1}} - \eta D_L^{(m)}(\widetilde{L}, \widetilde{G}, \widetilde{H})\,, \qquad \dot{\widetilde{G}} = -\eta D_G^{(m)}(\widetilde{L}, \widetilde{G}, \widetilde{H})\,, \qquad \dot{\widetilde{H}} = -\eta D_H^{(m)}(\widetilde{L}, \widetilde{G}, \widetilde{H})\,,$$

$$(5.7)$$

where the dissipative effects are described by the time depending parameter $\eta = \rho B$ and the functions $D_L^{(m)}$, $D_G^{(m)}$, $D_H^{(m)}$ are defined as

$$
\begin{aligned}
D_L^{(m)}(\widetilde{L}, \widetilde{G}, \widetilde{H}) &= \frac{\mu_E}{2}\left(1 - \frac{\omega_E \widetilde{L}^3(\widetilde{H} + m\widetilde{L})}{\mu_E^2(\widetilde{G} + \widetilde{L})}\right)^2 , \\
D_G^{(m)}(\widetilde{L}, \widetilde{G}, \widetilde{H}) &= \frac{\widetilde{G}}{\widetilde{L}} D_L^{(m)}(\widetilde{L}, \widetilde{G}, \widetilde{H}) , \\
D_H^{(m)}(\widetilde{L}, \widetilde{G}, \widetilde{H}) &= \frac{\widetilde{H}}{\widetilde{L}} D_L^{(m)}(\widetilde{L}, \widetilde{G}, \widetilde{H}) .
\end{aligned}
\tag{5.8}
$$

Since η is a small quantity, from (5.7), it follows that $\widetilde{G}$ and $\widetilde{H}$ modify slightly in time, due to the effect of the dissipation. Being interested in equilibria located in the $(\sigma_{m1}, \widetilde{L})$ plane, and also in obtaining a very reduced model apt to explore the dynamics of infinitesimal bodies close to resonances, we define a *dissipative toy model* governed by the following differential equations:

$$
\begin{aligned}
\dot{\sigma}_{m1} &= \widetilde{h}_{,L}^{(m)}(\widetilde{L}, \widetilde{G}, \widetilde{H}) + \varepsilon \widetilde{\mathcal{A}}_{,L}^{(m)}(\widetilde{L}, \widetilde{G}, \widetilde{H}) \ \cos(\sigma_{m1} - \widetilde{\varphi}^{(m)}(\widetilde{G}, \widetilde{H})) , \\
\dot{\widetilde{L}} &= \varepsilon \widetilde{\mathcal{A}}^{(m)}(\widetilde{L}, \widetilde{G}, \widetilde{H}) \sin(\sigma_{m1} - \widetilde{\varphi}^{(m)}(\widetilde{G}, \widetilde{H})) - \eta D_L^{(m)}(\widetilde{L}, \widetilde{G}, \widetilde{H}) ,
\end{aligned}
\tag{5.9}
$$

where $\widetilde{G}$ and $\widetilde{H}$ are considered constants; let us stress this aspect by replacing them in the following by $\widetilde{G}_0$ and $\widetilde{H}_0$. Also, we will use the customary differentiation convention stating that subscripts preceded by a comma denote partial differentiation with respect to the corresponding variable.

Since the main goal of this section is to present a qualitative description of the interplay between the resonances and the dissipative effects (including the existence, type and location of the equilibrium points as a function of various parameters), we shall consider the parameter η as a constant, leaving to Section 6 the study of the case of a variable η, which corresponds to study the effects of the solar cycle.

In order to validate the toy model and to show numerically the existence of the equilibrium points, we present in Figure 3 some results obtained by using the DMLR described in the previous sections, including also the air resistance effect for the 12:1, 13:1 and 14:1 resonances. Plotting the Fast Lyapunov Indicator[1], hereafter denoted as FLI (see, e.g, Froeschlé et al. (1997); Guzzo et al. (2002); Guzzo & Lega (2013); Celletti & Galeş (2014)) for some given values of the parameters (i.e. eccentricity, inclination, ballistic coefficient, etc.), we can infer a very good agreement between the equilibria of the toy

---

[1]The Fast Lyapunov Indicator is a measure of the regular and chaotic dynamics; it was introduced in Froeschlé et al. (1997) and it amounts, in short, to the Lyapunov exponent computed on finite times.

model and those of the DMLR. Indeed, the equilibrium points are clearly revealed for small dissipations (or for the non–dissipative case of the 11:1 resonance), the resonant islands have the amplitude as predicted by the conservative toy model (compare with Figures 2 and 3) and, as we will see in the next sections, the dissipative toy model is able to predict the existence and location of the equilibrium points.

Since the upper left panel of Figure 3 is obtained for a conservative model, more precisely a pendulum-type Hamiltonian, the stable and unstable points, as well as the separatrix are clearly marked. Since the other plots of Figure 3 take also into account the dissipative effect, the separatrix of each plot is not longer a single line, as for a conservative system; the gradual decrease of the orbits' altitude due to dissipation leads the paths located above the resonant region to reach, after some time, the separatrix. This is the reason why in all other plots of Figure 3 we notice a larger chaotic region above the resonant island, than below it. The plots are obtained by integrating the equations of motion for an interval of 1500 sidereal days. Due to the orbital decay process, a longer time span integration is considered, hence a much larger chaotic region is obtained above the resonant zone. Once an orbit reaches the resonant region, two scenarios are possible: either it passes through resonance, or it is captured into resonance. Numerical simulations show that the capture is a rare and temporary phenomenon, depending on different factors including that η varies in time as effect of the solar cycle (see Section 6). In any case, even if the object is captured temporarily by a resonance, it does not usually reach the center of the island, where the spiral point is located. Figure 4, obtained by using the DMLR, shows an example of the two different phenomena: a passage through the 14:1 resonance and a temporary capture in the 12:1 resonance.

5.2. **Existence of equilibrium points.** Using the toy model introduced in Section 5.1, we can prove the following result.

Theorem 4. *For fixed values of $e \in [0, 0.02]$ and $i \in [0^o, 120^o]$ (or equivalently, given $\widetilde{G}_0$ and $\widetilde{H}_0$ in the corresponding intervals), let $(\sigma_{m1}^{(0)}, \widetilde{L}_0)$ be an equilibrium point for the model described by the Hamiltonian (5.5). Let $\widetilde{\mathcal{A}}^{(m)}$ be as in (5.6) and $D_L^{(m)}$ as in (5.8); assume that η, ε satisfy the inequalities:*

$$\left| \frac{\eta D_L^{(m)}(\widetilde{L}_0, \widetilde{G}_0, \widetilde{H}_0)}{\varepsilon \widetilde{\mathcal{A}}^{(m)}(\widetilde{L}_0, \widetilde{G}_0, \widetilde{H}_0)} \right| + \frac{2\varepsilon \left(\widetilde{\mathcal{A}}_{,L}^{(m)}(\widetilde{L}_0, \widetilde{G}_0, \widetilde{H}_0) \right)^2 + 2\eta \left| \widetilde{\mathcal{A}}_{,L}^{(m)}(\widetilde{L}_0, \widetilde{G}_0, \widetilde{H}_0) D_{L,L}^{(m)}(\widetilde{L}_0, \widetilde{G}_0, \widetilde{H}_0) \right) \right|}{|\widetilde{h}_{,LL}^{(m)}(\widetilde{L}_0, \widetilde{G}_0, \widetilde{H}_0)| \; \widetilde{\mathcal{A}}^{(m)}(\widetilde{L}_0, \widetilde{G}_0, \widetilde{H}_0)} \leq 1 - \delta \,,$$

$$\varepsilon^2 < \gamma \, \delta \qquad\qquad\qquad (5.10)$$
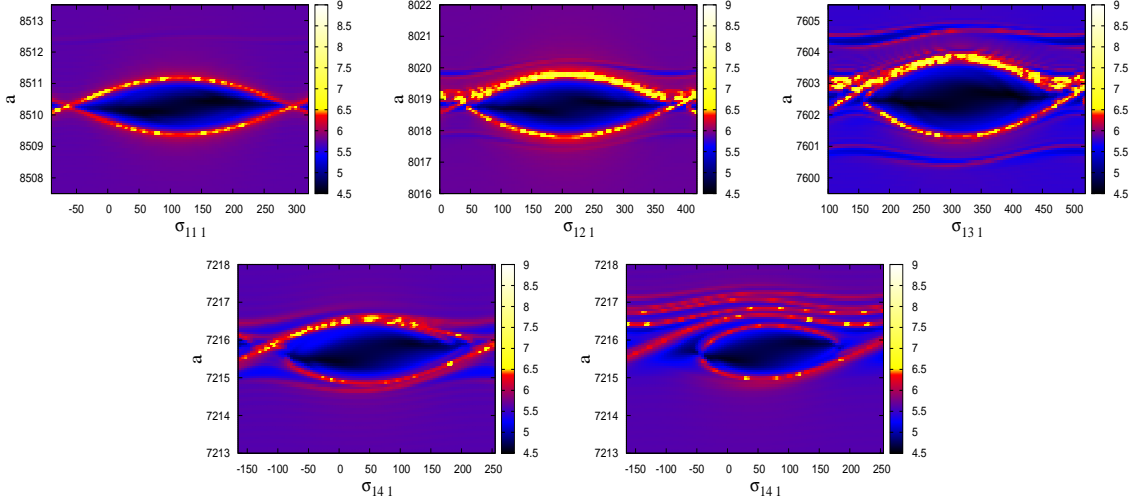
FIGURE 3. FLI (using the DMLR) for the 11:1, 12:1, 13:1, 14:1
resonances for $e = 0.005$, $\omega = 0^o$, $\Omega = 0^o$. Top left: 11:1 resonance for
$i = 80^o$; top middle: 12:1 resonance for $i = 70^o$, mean atmospheric density
and $B = 220$ $[cm^2/kg]$; top right: 13:1 resonance for $i = 75^o$, mean
atmospheric density and $B = 220$ $[cm^2/kg]$; bottom: 14:1 resonance for
$i = 60^o$, mean atmospheric density and $B = 30$ $[cm^2/kg]$ (left panel),
respectively $B = 220$ $[cm^2/kg]$ (right panel). The time span is 1500
sidereal days (about 4 years).

*for some constants $0 < \delta < 1$ and $\gamma > 0$. Then, the dissipative toy model described by the
equations (5.9) admits equilibrium points. At first order in η, the point $(\sigma_{m1}^{(1)}, \widetilde{L}_1)$ defined
by*

$$\sigma_{m1}^{(1)} = \sigma_{m1}^{(0)} + \frac{D_{,L}^{(m)}(\widetilde{L}_0, \widetilde{G}_0, \widetilde{H}_0)}{\varepsilon \widetilde{\mathcal{A}}^{(m)}(\widetilde{L}_0, \widetilde{G}_0, \widetilde{H}_0)\cos(\sigma_{m1}^0 - \widetilde{\varphi}^{(m)})}\eta \ , \qquad \widetilde{L}_1 = \widetilde{L}_0 \qquad (5.11)$$

is an equilibrium point for the dissipative model.

Proof. Since $(\sigma_{m1}^{(0)}, \widetilde{L}_0)$ is an equilibrium point for the conservative model (5.5), one
has

$$\widetilde{h}_{,L}^{(m)}(\widetilde{L}_0, \widetilde{G}_0, \widetilde{H}_0) + \varepsilon \widetilde{\mathcal{A}}_{,L}^{(m)}(\widetilde{L}_0, \widetilde{G}_0, \widetilde{H}_0)\cos(\sigma_{m1}^{(0)} - \widetilde{\varphi}^{(m)}(\widetilde{G}_0, \widetilde{H}_0)) = 0 \ ,$$
$$\sin(\sigma_{m1}^{(0)} - \widetilde{\varphi}^{(m)}(\widetilde{G}_0, \widetilde{H}_0)) = 0 \ . \qquad (5.12)$$

The relations (5.12) represent an uncoupled system of two equations. The second of
(5.12) provides two values for $\sigma_{m1}^{(0)}$ in the interval $[0^o, 360^o)$. Once $\sigma_{m1}^{(0)}$ is known, $\widetilde{L}_0$ is
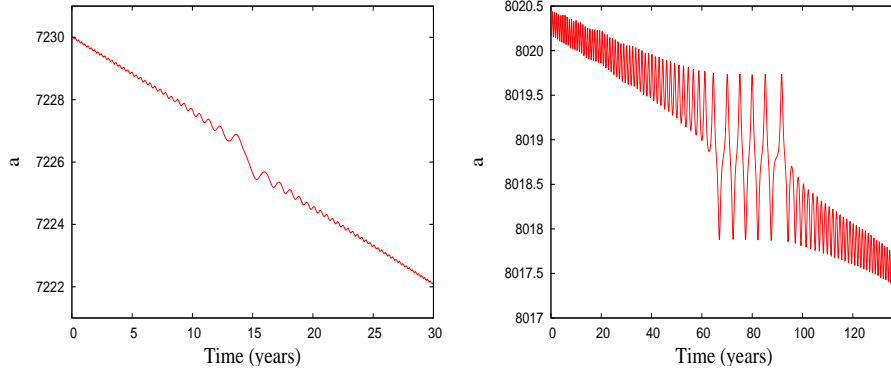found by solving the first of (5.12) for fixed values of $\widetilde{G}_0, \widetilde{H}_0$.

FIGURE 4. Passage through the 14:1 resonance (left) and temporary capture into the 12:1 resonance (right). The plots are obtained for $e = 0.005$, $i = 70^o$, $\omega = 0^o$, $\Omega = 0^o$, $\sigma_{m1} = 100^o$ and $B = 220$ $[cm^2/kg]$.

It is important to stress that, since ε is small, $\widetilde{L}_0$ has the form $\widetilde{L}_0 = \widetilde{L}^{sec} + \varepsilon L_0^* + O(\varepsilon^2)$, where L_0^* is independent of ε and $\widetilde{L}^{sec}$ satisfies the equation

$$\widetilde{h}_{,L}^{(m)}(\widetilde{L}^{sec}, \widetilde{G}_0, \widetilde{H}_0) = 0 \ .$$

Inserting $\widetilde{L}_0 = \widetilde{L}^{sec} + \varepsilon L_0^* + O(\varepsilon^2)$ in the first of (5.12) and expanding to the first order in ε, we find that $\widetilde{L}_0$ has the form

$$\widetilde{L}_0 = \widetilde{L}^{sec} \pm \varepsilon \ \frac{\widetilde{\mathcal{A}}_{,L}^{(m)}(\widetilde{L}^{sec}, \widetilde{G}_0, \widetilde{H}_0)}{\widetilde{h}_{,LL}^{(m)}(\widetilde{L}^{sec}, \widetilde{G}_0, \widetilde{H}_0)} + O(\varepsilon^2) \ , \tag{5.13}$$

where the signs $\pm$ correspond to the two solutions of the second of (5.12). In obtaining (5.13), we took into account the fact that $\widetilde{h}^{(m)}$ in (5.6) assures that $\widetilde{h}_{,LL}^{(m)}$ cannot be zero for the resonances and parameter values considered in this work (notably, J_2 is sufficiently small).

On the other hand, for the dissipative toy model we have the following coupled equations for the determination of an equilibrium point, say $(\sigma_{m1}^{(d)}, \widetilde{L}_d)$:

$$\widetilde{h}_{,L}^{(m)}(\widetilde{L}_d, \widetilde{G}_0, \widetilde{H}_0) + \varepsilon\widetilde{\mathcal{A}}_{,L}^{(m)}(\widetilde{L}_d, \widetilde{G}_0, \widetilde{H}_0)\cos(\sigma_{m1}^{(d)} - \widetilde{\varphi}^{(m)}(\widetilde{G}_0, \widetilde{H}_0)) \ = \ 0 \ ,$$
$$\varepsilon\widetilde{\mathcal{A}}^{(m)}(\widetilde{L}_d, \widetilde{G}_0, \widetilde{H}_0)\sin(\sigma_{m1}^{(d)} - \widetilde{\varphi}^{(m)}(\widetilde{G}_0, \widetilde{H}_0)) - \eta D_L^{(m)}(\widetilde{L}_d, \widetilde{G}_0, \widetilde{H}_0) \ = \ 0 \ . \tag{5.14}$$

The first of (5.14) can always be satisfied; that is, for any value of $\sigma_{m1}^{(d)}$ in the interval $[0^o, 360^o)$ we may find a value $\widetilde{L}_d$ which verifies this equation. However, the second of (5.14) is satisfied only if the dissipative effects do not exceed a threshold value. To show this, let us fix an arbitrary value for $\sigma_{m1}^{(d)}$ in the interval $[0^o, 360^o)$ and let $\widetilde{L}_d^{\sigma}$ be such that

$(\sigma_{m1}^{(d)}, \widetilde{L}_d^\sigma)$ satisfies the first of (5.14). Using the same argument as the one used to obtain (5.13), we deduce that $\widetilde{L}_d^\sigma$ has the form

$$\widetilde{L}_d^\sigma = \widetilde{L}^{sec} - \varepsilon \, \frac{\widetilde{\mathcal{A}}_{,L}^{(m)}(\widetilde{L}^{sec}, \widetilde{G}_0, \widetilde{H}_0) \cos(\sigma_{m1}^{(d)} - \widetilde{\varphi}^{(m)}(\widetilde{G}_0, \widetilde{H}_0))}{\widetilde{h}_{,LL}^{(m)}(\widetilde{L}^{sec}, \widetilde{G}_0, \widetilde{H}_0)} + O(\varepsilon^2) \,. \tag{5.15}$$

Now, we note that if f is a differentiable function of $\widetilde{L}$, then in view of the relation $\widetilde{L}^{sec} = \widetilde{L}_0 - \varepsilon L_0^* + O(\varepsilon^2)$, we can write $f(\widetilde{L}^{sec}) = f(\widetilde{L}_0) - \varepsilon L_0^* \, f_{,L}(\widetilde{L}_0) + O(\varepsilon^2)$. Using this argument, from (5.13) and (5.15) we get

$$\widetilde{L}_d^\sigma = \widetilde{L}_0 - \varepsilon \, \frac{\widetilde{\mathcal{A}}_{,L}^{(m)}(\widetilde{L}_0, \widetilde{G}_0, \widetilde{H}_0) \Big(\cos(\sigma_{m1}^{(d)} - \widetilde{\varphi}^{(m)}(\widetilde{G}_0, \widetilde{H}_0)) \mp 1 \Big)}{\widetilde{h}_{,LL}^{(m)}(\widetilde{L}_0, \widetilde{G}_0, \widetilde{H}_0)} + O(\varepsilon^2) \,. \tag{5.16}$$

Inserting $\widetilde{L}_d^\sigma$ given by (5.16) in the second of (5.14), then after some computations we get the following equation for the unknown variable $\sigma_{m1}^{(d)}$

$$\sin(\sigma_{m1}^{(d)} - \widetilde{\varphi}^{(m)}) = \frac{\eta D_L^{(m)}}{\varepsilon \widetilde{\mathcal{A}}^{(m)}} + \frac{\widetilde{\mathcal{A}}_{,L}^{(m)} \Big(\cos(\sigma_{m1}^{(d)} - \widetilde{\varphi}^{(m)}) \mp 1 \Big)}{\widetilde{h}_{,LL}^{(m)} \widetilde{\mathcal{A}}^{(m)}} \Big(\varepsilon \widetilde{\mathcal{A}}_{,L}^{(m)} \sin(\sigma_{m1}^{(d)} - \widetilde{\varphi}^{(m)}) - \eta D_{L,L}^{(m)} \Big) + O(\varepsilon^2) \,, \tag{5.17}$$

where all functions are evaluated at $\widetilde{L}_0, \widetilde{G}_0, \widetilde{H}_0$. In view of (5.10), bounding the terms of second order in ε by $C_0 \varepsilon^2$ for a suitable constant $C_0 > 0$, we have

$$\left| \frac{\eta D_L^{(m)}}{\varepsilon \widetilde{\mathcal{A}}^{(m)}} + \frac{\widetilde{\mathcal{A}}_{,L}^{(m)} \Big(\cos(\sigma_{m1}^{(d)} - \widetilde{\varphi}^{(m)}) \mp 1 \Big)}{\widetilde{h}_{,LL}^{(m)} \widetilde{\mathcal{A}}^{(m)}} \Big(\varepsilon \widetilde{\mathcal{A}}_{,L}^{(m)} \sin(\sigma_{m1}^{(d)} - \widetilde{\varphi}^{(m)}) - \eta D_{L,L}^{(m)} \Big) \right| + C_0 \varepsilon^2$$

$$\leq \left| \frac{\eta D_L^{(m)}}{\varepsilon \widetilde{\mathcal{A}}^{(m)}} \right| + \frac{2\varepsilon \Big(\widetilde{\mathcal{A}}_{,L}^{(m)} \Big)^2 + 2\eta |\widetilde{\mathcal{A}}_{,L}^{(m)} D_{L,L}^{(m)}|}{|\widetilde{h}_{,LL}^{(m)}| \, \widetilde{\mathcal{A}}^{(m)}} + C_0 \varepsilon^2 \leq 1 - \delta + C_0 \varepsilon^2 \leq 1 \,,$$

for ε sufficiently small with respect to δ as in the second of (5.10) with $\gamma \equiv 1/C_0$. Therefore, if (5.10) are satisfied, then the right hand side of (5.17) is subunitary, which implies that the dissipative toy model admits equilibrium points.

Assuming that η is sufficiently small, so that (5.10) holds, then at first order in η, it is natural to look for an equilibrium point of the dissipative toy model (5.9) of the type $(\sigma_{m1}^{(1)}, \widetilde{L}_1)$, where

$$\sigma_{m1}^{(1)} = \sigma_{m1}^{(0)} + \eta \sigma_{m1}^* + O(\eta^2) \,, \qquad \widetilde{L}_1 = \widetilde{L}_0 + \eta L^* + O(\eta^2) \tag{5.18}$$

with L^* and σ_{m1}^* independent of η. In fact, we shall suppose that η is smaller than ε, ensuring thus that $\sigma_{m1}^{(1)}$ is close to $\sigma_{m1}^{(0)}$. As a consequence, if g is a differentiable function

of σ_{m1}, then it follows that $g(\sigma_{m1}^{(1)}) = g(\sigma_{m1}^{(0)}) + \eta\sigma_{m1}^* \, g_{,\sigma}(\sigma_{m1}^{(0)}) + O(\eta^2)$. Inserting (5.18) in the right hand side of (5.9) and using (5.12), we obtain after some computations:

$$
\begin{aligned}
&\widetilde{h}_{,L}^{(m)}(\widetilde{L}_1, \widetilde{G}_0, \widetilde{H}_0) + \varepsilon\widetilde{\mathcal{A}}_{,L}^{(m)}(\widetilde{L}_1, \widetilde{G}_0, \widetilde{H}_0)\cos(\sigma_{m1}^{(1)} - \widetilde{\varphi}^{(m)}(\widetilde{G}_0, \widetilde{H}_0)) \\
&= \eta[\widetilde{h}_{,LL}^{(m)}(\widetilde{L}_0, \widetilde{G}_0, \widetilde{H}_0) + \varepsilon\widetilde{\mathcal{A}}_{,LL}^{(m)}(\widetilde{L}_0, \widetilde{G}_0, \widetilde{H}_0)\cos(\sigma_{m1}^{(0)} - \widetilde{\varphi}^{(m)}(\widetilde{G}_0, \widetilde{H}_0))]L^* + O(\eta^2)\,, \\
&\varepsilon\widetilde{\mathcal{A}}^{(m)}(\widetilde{L}_1, \widetilde{G}_0, \widetilde{H}_0)\sin(\sigma_{m1}^{(1)} - \widetilde{\varphi}^{(m)}(\widetilde{G}_0, \widetilde{H}_0)) - \eta D_L^{(m)}(\widetilde{L}_1, \widetilde{G}_0, \widetilde{H}_0) \\
&= \eta[\varepsilon\widetilde{\mathcal{A}}^{(m)}(\widetilde{L}_0, \widetilde{G}_0, \widetilde{H}_0)\sigma_{m1}^*\cos(\sigma_{m1}^{(0)} - \widetilde{\varphi}^{(m)}(\widetilde{G}_0, \widetilde{H}_0)) - D_L^{(m)}(\widetilde{L}_0, \widetilde{G}_0, \widetilde{H}_0)] + O(\eta^2)\,.
\end{aligned}
\tag{5.19}
$$

Taking into account that ε is a small parameter, it follows that the quantity in brackets at the right hand side of the first of (5.19) is different from zero for ε sufficiently small. Therefore, for $(\sigma_{m1}^{(1)}, \widetilde{L}_1)$ to be an equilibrium point (at first order in η) for the dissipative toy model, one should have $L^* = 0$ and, consequently,

$$
\sigma_{m1}^* = \frac{D_L^{(m)}(\widetilde{L}_0, \widetilde{G}_0, \widetilde{H}_0)}{\varepsilon\widetilde{\mathcal{A}}^{(m)}(\widetilde{L}_0, \widetilde{G}_0, \widetilde{H}_0)\cos(\sigma_{m1}^{(0)} - \widetilde{\varphi}^{(m)}(\widetilde{L}_0, \widetilde{G}_0, \widetilde{H}_0))}\,.
\tag{5.20}
$$

From (5.18) and (5.20), we get (5.11). $\square$

Remark 5. *Since ε and η are small (for instance, for the 14:1 resonance the parameter ε is of the order of 10^{-9}, while η is smaller than ε), the existence condition can be replaced by the following simplified inequality*

$$
\left| \frac{\eta D_L^{(m)}(\widetilde{L}_0, \widetilde{G}_0, \widetilde{H}_0)}{\varepsilon\widetilde{\mathcal{A}}^{(m)}(\widetilde{L}_0, \widetilde{G}_0, \widetilde{H}_0)} \right| \leq 1 - \delta\,,
$$

where ε and η satisfy the relation

$$
\gamma_1\varepsilon + \gamma_2\eta + \gamma_3\varepsilon^2 < \delta,
$$

for some positive constants γ_1, γ_2 and γ_3.

Besides the existence condition (5.10), Theorem 4 shows that a change in magnitude of the dissipative effects leads to a shift of the equilibrium points on the σ_{m1} axis, $\widetilde{L}$ (or equivalently the semimajor axis a) remaining unchanged. Indeed, in the bottom panels of Figure 3, obtained for $B = 30\,[cm^2/kg]$ (left) and $B = 220\,[cm^2/kg]$ (right), the centers of the islands are located at about $\sigma_{14,1} = 48^o$ and $\sigma_{14,1} = 60^o$, respectively, revealing thus the shift of equilibrium points on the $\sigma_{14,1}$ axis, while confirming that the value of $\widetilde{L}$ at equilibrium does not change.

5.3. **Type of equilibrium points.** In Section 5.2 we investigated the existence of equilibrium points without specifying their character. Since the conservative toy model reduces to a pendulum problem, the equilibrium points are centers and saddles. Therefore, it remains to clarify the nature of equilibria for the dissipative toy model. The link between the character of the equilibria in the conservative and dissipative frameworks is given by the following result.

Theorem 6. *For given values of $\widetilde{G}_0$ and $\widetilde{H}_0$, let $(\sigma_{m1}^{(0)}, \widetilde{L}_0)$, $m \in \{11, 12, 13, 14\}$, be an equilibrium point for the conservative toy model described by the Hamiltonian (5.5), satisfying (5.10) for some $\delta > 0$, $0 < \varepsilon < 1$. Assume that the existence condition (5.10) is satisfied and that $\eta < \varepsilon$. Then, the following statement holds true: if $(\sigma_{m1}^{(0)}, \widetilde{L}_0)$ is a center (respectively a saddle) for the conservative toy model, then the equilibrium point at first order in η, say $(\sigma_{m1}^{(1)}, \widetilde{L}_1)$, defined by (5.11) is an unstable spiral (respectively a saddle) for the dissipative toy model described by (5.9).*

Proof. Using (5.12), the Jacobian matrix associated to the conservative case has the form:

$$J_C = \begin{pmatrix} 0 & \widetilde{h}_{,LL}^{(m)} + \varepsilon \widetilde{\mathcal{A}}_{,LL}^{(m)} \cos(\sigma_{m1}^{(0)} - \widetilde{\varphi}^{(m)}) \\ \varepsilon \widetilde{\mathcal{A}}^{(m)} \cos(\sigma_{m1}^{(0)} - \widetilde{\varphi}^{(m)}) & 0 \end{pmatrix},$$

where all functions are computed at $(\widetilde{L}_0, \widetilde{G}_0, \widetilde{H}_0)$. Since ε is a small parameter and $\widetilde{h}^{(m)}(\widetilde{L}_0, \widetilde{G}_0, \widetilde{H}_0)$, $\widetilde{\mathcal{A}}^{(m)}(\widetilde{L}_0, \widetilde{G}_0, \widetilde{H}_0)$ have the same order of magnitude, the sign of $\det(J_C)$ is given by the expression $-\varepsilon \widetilde{h}_{,LL}^{(m)}(\widetilde{L}_0, \widetilde{G}_0, \widetilde{H}_0) \widetilde{\mathcal{A}}^{(m)}(\widetilde{L}_0, \widetilde{G}_0, \widetilde{H}_0) \cos(\sigma_{m1}^{(0)} - \widetilde{\varphi}^{(m)}(\widetilde{L}_0, \widetilde{G}_0, \widetilde{H}_0))$, provided ε is sufficiently small. Moreover, taking into account that $\widetilde{h}_{,LL}^{(m)}(\widetilde{L}_0, \widetilde{G}_0, \widetilde{H}_0) < 0$ (provided α in (5.6) is sufficiently small) and (as we mentioned in Section 3.1.2) $\widetilde{\mathcal{A}}^{(m)}(\widetilde{L}_0, \widetilde{G}_0, \widetilde{H}_0) > 0$, then for $\sigma_{m1}^{(0)} = \widetilde{\varphi}^{(m)}(\widetilde{L}_0, \widetilde{G}_0, \widetilde{H}_0) + 2k\pi$, $k \in \mathbb{Z}$, one has that $\det(J_C) > 0$. As a consequence, $(\sigma_{m1}^{(0)}, \widetilde{L}_0)$ is a center, while for $\sigma_{m1}^{(0)} = \widetilde{\varphi}^{(m)} + \pi + 2k\pi$, $k \in \mathbb{Z}$, the equilibrium point $(\sigma_{m1}^{(0)}, \widetilde{L}_0)$ is a saddle.

Assuming that the existence condition (5.10) is satisfied, then for the dissipative case, the Jacobian matrix is

$$J_D = \begin{pmatrix} -\varepsilon \widetilde{\mathcal{A}}_{,L}^{(m)} \sin(\sigma_{m1}^{(1)} - \widetilde{\varphi}^{(m)}) & \widetilde{h}_{,LL}^{(m)} + \varepsilon \widetilde{\mathcal{A}}_{,LL}^{(m)} \cos(\sigma_{m1}^{(1)} - \widetilde{\varphi}^{(m)}) \\ \varepsilon \widetilde{\mathcal{A}}^{(m)} \cos(\sigma_{m1}^{(1)} - \widetilde{\varphi}^{(m)}) & \varepsilon \widetilde{\mathcal{A}}_{,L}^{(m)} \sin(\sigma_{m1}^{(1)} - \widetilde{\varphi}^{(m)}) - \eta D_{L,L}^{(m)} \end{pmatrix}, \quad (5.21)$$

where all functions are evaluated at $\widetilde{L}_1, \widetilde{G}_0, \widetilde{H}_0$.

Using that η is smaller than ε (thus ensuring that $\sigma_{m1}^{(1)}$ is close to $\sigma_{m1}^{(0)}$), then if f and g are two differentiable functions of $\widetilde{L}$ and σ_{m1}, respectively, in view of (5.18) and the fact

that $L^* = 0$, we can write

$$f(\widetilde{L}_1) = f(\widetilde{L}_0) + f_{,L}(\widetilde{L}_0)(\widetilde{L}_1 - \widetilde{L}_0) + O(\eta^2) = f(\widetilde{L}_0) + O(\eta^2)$$

$$g(\sigma_{m1}^{(1)}) = g(\sigma_{m1}^{(0)}) + g_{,\sigma}(\sigma_{m1}^{(0)})(\sigma_{m1}^{(1)} - \sigma_{m1}^{(0)}) + O(\eta^2) = g(\sigma_{m1}^{(0)}) + \eta g_{,\sigma}(\sigma_{m1}^{(0)})\sigma_{m1}^* + O(\eta^2).$$

$$(5.22)$$

From (5.12), (5.21) and (5.22) it follows that (tr is the trace of the matrix and det its determinant)

$$tr(J_D) = -\eta D_{L,L}^{(m)} + O(\eta^2),$$

$$\det(J_D) = -\varepsilon \widetilde{h}_{,LL}^{(m)}\mathcal{A}^{(m)}\cos(\sigma_{m1}^{(0)} - \widetilde{\varphi}^{(m)}) + O(\eta\varepsilon) + O(\eta^2) + O(\varepsilon^2),$$

$$\left(tr(J_D)\right)^2/4 - \det(J_D) = \varepsilon \widetilde{h}_{,LL}^{(m)}\mathcal{A}^{(m)}\cos(\sigma_{m1}^{(0)} - \widetilde{\varphi}^{(m)}) + O(\eta\varepsilon) + O(\eta^2) + O(\varepsilon^2),$$

where all functions are evaluated at $\widetilde{L}_0$, $\widetilde{G}_0$, $\widetilde{H}_0$. In order to establish the nature of the equilibrium point $(\sigma_{m1}^{(1)}, \widetilde{L}_1)$, we must know the sign of the above quantities. Therefore, let us discuss in more detail the sign of $D_{L,L}^{(m)}$. In view of the first of (5.8), we get

$$D_{L,L}^{(m)} = -\frac{\omega_E}{\mu_E}\left(1 - \frac{\omega_E \widetilde{L}_0^3(\widetilde{H}_0 + m\widetilde{L}_0)}{\mu_E^2(\widetilde{G}_0 + \widetilde{L}_0)}\right)\frac{[3\widetilde{L}_0^2(\widetilde{H}_0 + m\widetilde{L}_0) + m\widetilde{L}_0^3](\widetilde{G}_0 + \widetilde{L}_0) - \widetilde{L}_0^3(\widetilde{H}_0 + m\widetilde{L}_0)}{(\widetilde{G}_0 + \widetilde{L}_0)^2}.$$

$$(5.23)$$

To evaluate the sign of the above expression, we take into account that the eccentricity is a small quantity, say $e = O(\epsilon)$ with ϵ small. Therefore, from (2.1) and (5.4), it follows that $\widetilde{G}_0 = O(\epsilon)$, $\widetilde{H}_0 = \widetilde{L}_0(\cos i - m) + O(\epsilon)$, which leads to

$$[3\widetilde{L}_0^2(\widetilde{H}_0 + m\widetilde{L}_0) + m\widetilde{L}_0^3](\widetilde{G}_0 + \widetilde{L}_0) - \widetilde{L}_0^3(\widetilde{H}_0 + m\widetilde{L}_0) = \widetilde{L}_0^4(2\cos i + m) + O(\epsilon) > 0$$

for $m > 2$. Since the term in round brackets at the right hand side of (5.23) is positive for all resonances within the geostationary distance, we deduce that $D_{L,L}^{(m)}$ is negative and, as a consequence, $tr(J_D)$ is positive, provided η is sufficiently small.

We are therefore led to the following conclusion. If $(\sigma_{m1}^{(0)}, \widetilde{L}_0)$ is a center for the conservative model and using that η is smaller than ε (thus ensuring that $\sigma_{m1}^{(1)}$ is close to $\sigma_{m1}^{(0)}$), then one has $tr(J_D) > 0$, $\det(J_D) > 0$, $\left(tr(J_D)\right)^2/4 - \det(J_D) < 0$ and, as a consequence, $(\sigma_{m1}^{(1)}, \widetilde{L}_1)$ is an unstable spiral for the dissipative toy model. Otherwise, if $(\sigma_{m1}^{(0)}, \widetilde{L}_0)$ is a saddle for the conservative model, then $\det(J_D) < 0$, $\left(tr(J_D)\right)^2/4 - \det(J_D) > 0$, which means that $(\sigma_{m1}^{(1)}, \widetilde{L}_1)$ is a saddle point for the dissipative toy model. $\square$

5.4. **Location of equilibrium points.** Using the toy model introduced in Section 5.1, we investigate the existence and location of the equilibrium points for each resonance and for all values of eccentricity, inclination, ballistic coefficient and atmospheric density.
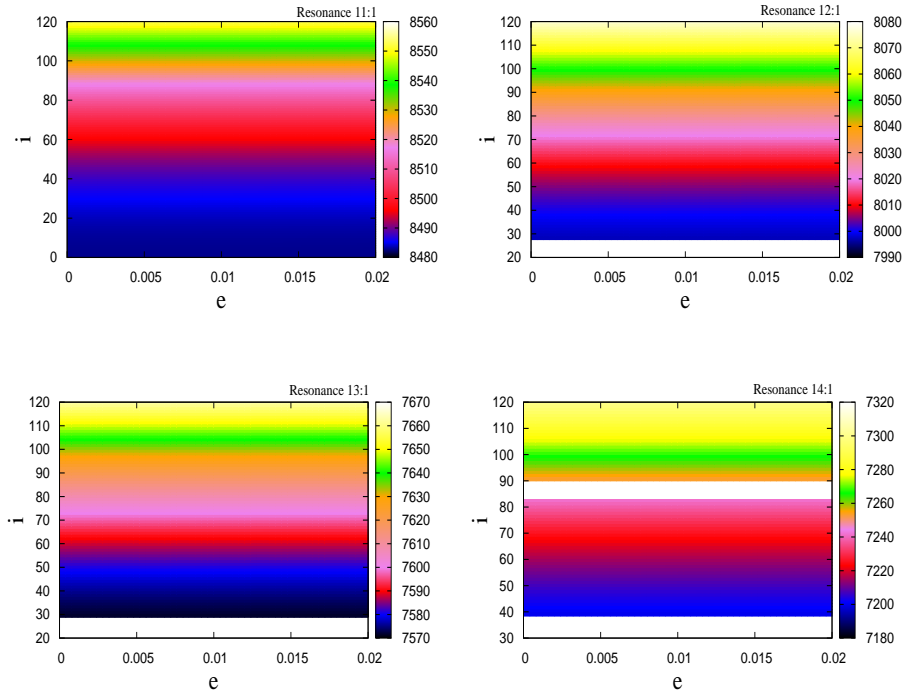
FIGURE 5. Position of the equilibrium points obtained using (5.11) on the semi-major axis as a function of eccentricity and inclination. The color bar provides the distance of the equilibrium points from the Earth's center. From top left to bottom right: 11:1, 12:1, 13:1, 14:1 resonances. Excluding the 11:1 resonance obtained within the conservative case, all other plots are given for $B = 220 \, [cm^2/kg]$ and mean values of the atmospheric density. For the white zones, the existence condition (5.10) is not satisfied, which implies that the equilibrium points do not exist.

We should stress that, although all equilibria are unstable for the dissipative model, the instability effects are small in the case of spiral points, in the sense that a body placed close to this point will remain a long time in a neighborhood. This will become evident in Section 6 where various simulations are presented.

We report in Figures 5, 6 the locations of the semimajor axis and the values of the angles σ_{m1} for the equilibrium points (the centers for the 11:1 resonance and the spiral points for the other resonances), as a function of eccentricity and inclination. The plots corresponding to the 11:1 resonance are obtained within the conservative framework, while all other plots are obtained by using the dissipative toy model with $B = 220 \, [cm^2/kg]$ and for mean values of the atmospheric density. The white color in Figures 5, 6 shows
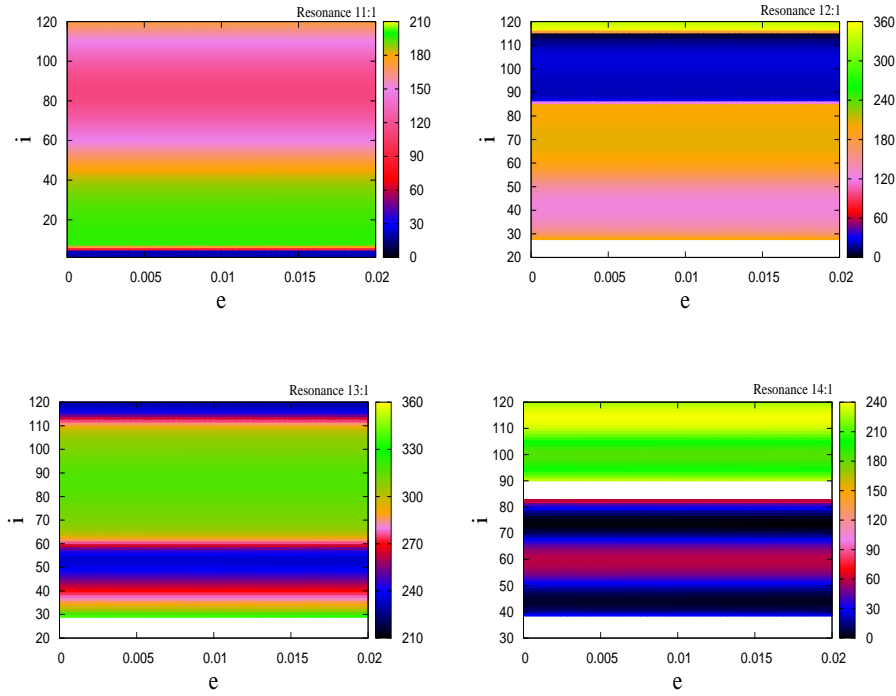
FIGURE 6. Location the equilibrium points (centers for the 11:1 resonance and spirals for the other resonances) on the σ_{m1} axis obtained using (5.11). The color bar provides the position of equilibria in degrees. From top left to bottom right: 11:1, 12:1, 13:1, 14:1 resonances. Excluding the 11:1 resonance obtained within the conservative setting, all other plots are derived for $B = 220 \, [cm^2/kg]$ and mean values of the atmospheric density. For the white zones, the existence condition (5.10) is not satisfied, which implies that the equilibrium points do not exist.

the regions for which the existence condition (5.10) is not satisfied. In other words, the dissipative effects are larger than the resonant ones, which implies that the equilibrium points do not exist.

Some transcritical bifurcation phenomena, as described in Celletti & Galeş (2014, 2015a), occur for the 12:1 and 14:1 resonances at $i_0 = 85.99^o$ and at $i_0 = 86.18^o$, respectively (see the location of the unstable spiral equilibrium points on the σ_{m1} axis close to these inclinations on the right plots of Figure 6). For example, in the case of the 14:1 resonance, the spiral point is located somewhere between 0° and 30° for $i \in [70^o, 80^o]$, while for $i > 90^o$ the position of the spiral point is close to 200°. A similar remark can be made for the resonance 12:1. The reason for the occurrence of this phenomenon is the
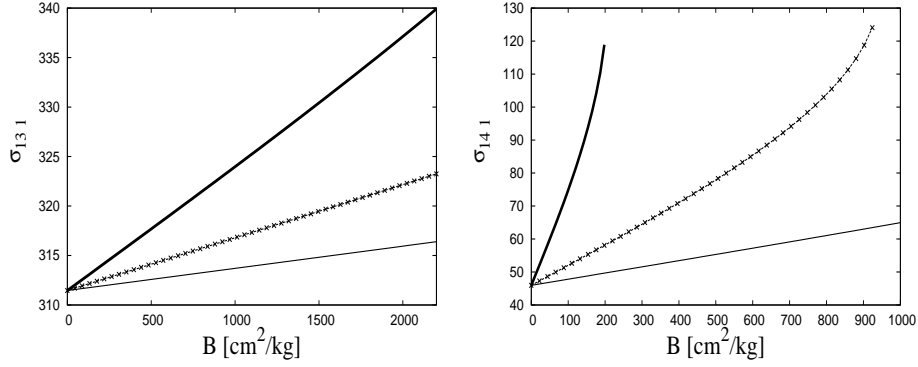
FIGURE 7. Location of the spiral equilibrium points on the σ_{m1} axis, expressed in degrees, as a function of the ballistic coefficient B. The thinner lines are obtained for minimum values of the atmospheric density, the dotted lines correspond to mean atmospheric densities, while the thicker curves provide the results for maximum values of the atmospheric density (see Table 3). Left: the 13:1 resonance for $i = 75^o$, $e = 0.005$, $\omega = 0^o$, $\Omega = 0^o$. Right: the 14:1 resonance for $i = 60^o$, $e = 0.005$, $\omega = 0^o$, $\Omega = 0^o$.

change of sign of a specific resonant term. More precisely, from the set $\mathcal{M}_0^{14}$, the resonant term with the largest magnitude at high inclinations is $\mathcal{T}_{15\,14\,7\,0}$. This term changes its sign, precisely at $i_0 = 86.18^o$. Therefore, in the neighborhood of i_0 it happens that for $i < i_0$ the spiral points are located close to the solution of $14\,\lambda_{15,14} - 90^o = 12^o$, while for $i > i_0$ the equilibrium points are located at about $\lambda_{15,14} = 192^o$. Of course, the equilibria are not located exactly at these positions, since $\mathcal{M}_0^{14}$ contains five terms, but very close to them. In the case of the 12:1 resonance, $\mathcal{T}_{15\,12\,7\,0}$ is the resonant term with the greatest magnitude for large inclinations and it changes its sign at $i_0 = 85.99^o$.

In view of Theorem 4, it follows that for increasing values of η (equivalently the ballistic coefficient and/or the atmospheric density) the white regions increase their area, while the *surviving* equilibria shift on the σ_{m1} axis. For each inclination and eccentricity, one can compute the maximum value of η up to which the inequality (5.10) is satisfied. In the case of the resonances 12:1 and 13:1, the simulations show that the existence condition (5.10) is usually fulfilled for inclinations larger than about 40°, even if the ballistic coefficient is large. On the other hand, since the atmospheric density is much larger at the altitude of $880\,km$, with notable variations during a solar cycle, the dissipative effect has an important contribution for the 14:1 resonance. Figure 7 shows the location of

spiral points on the σ_{m1} axis as a function of the ballistic coefficient, for minimum (thin line), mean (dotted curve) and maximum (thick curve) atmospheric density in the case of the 13:1 resonance, for $i = 75^o$ and $e = 0.005$, as well as for the 14:1 resonance when $i = 60^o$ and $e = 0.005$. The equilibrium points of (5.9) have been numerically obtained via the bisection method. For the 13:1 resonance, even though B varies on a large interval, all three curves are straight line segments. On the contrary, for the 14:1 resonance a curvature of the mean (dotted curve) and maximum (thick curve) atmospheric density is clearly visible for increasing values of B, thus pointing out the limits of the approximations (5.11), corresponding to the toy model. Besides, as the right panel of Figure 7 shows, the equilibrium points do not exist for $B > 200 \, cm^2/kg$ and a maximum value for ρ, and respectively for $B > 924 \, cm^2/kg$ and a medium value of the atmospheric density.

We remark that plots like those in Figure 7 can be used to analyze the shift of the equilibrium points on the σ_{m1} axis during a solar cycle. For instance, supposing that an infinitesimal body has the ballistic coefficient $B = 150 \, cm^2/kg$ then, within an interval of 11 years, the location of the spiral point varies between 48° and 92° for the 14:1 resonance, when $e = 0.005$ and $i = 60^o$. A satellite placed at, let say, $\sigma_{14\,1} = 70^o$ will stay very close to the spiral point, otherwise one should slightly correct its position to remain at the equilibrium point.

6. Solar cycle and third body effects

In this Section we consider a more complete model, which also takes into account the variation of the local density of the atmosphere as effect of the solar cycle, as well as the perturbations induced by Sun and Moon. We provide numerical evidence that the analytical results obtained in the previous Sections are valid when a more complete physical model is considered. In particular, we show that an object (satellite) placed at an equilibrium point remains there for a long time (of the order of dozens of years), even if solar cycle and third body effects are taken into account. Thus, we show a strong evidence that these points can be exploited in practice by parking satellites in their close vicinity. We exemplify just the case of the 14:1 resonance. Since the dissipative effects gradually decrease in magnitude with the altitude, for the other resonances studied in this paper the results are definitely better.

We suppose that the atmospheric density fluctuates with an 11-year cycle, as effect of the solar activity. To mimic the solar cycle, we shall use the following simple formula, which allows the density to vary periodically between its limits, minimum and maximum,
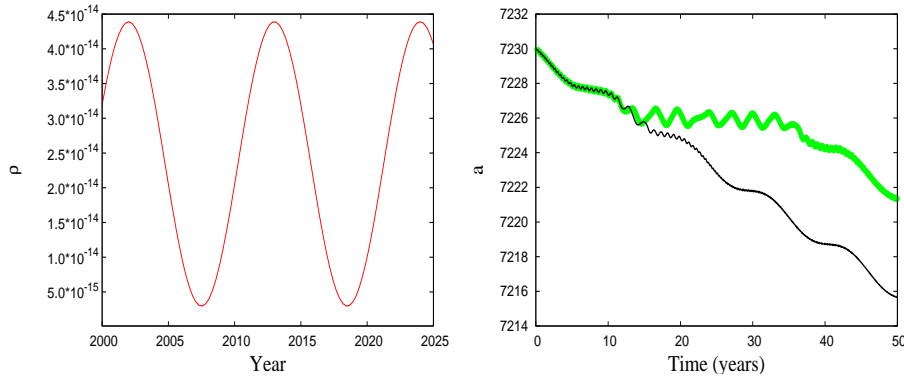
FIGURE 8. Left: variation of density in kg/m^3 at the altitude of 800 km, between the years 2000 and 2025, computed with the formula (6.1). Right: behavior of semi-major axis for $B = 100$ $[cm^2/kg]$ and the initial conditions $a = 7230$ km, $e = 0.005$, $i = 70^o$, $\omega = 0^o$, $\Omega = 0^o$ and $\sigma_{14\,1} = 80^0$. The results obtained for the model that disregards the influence of Sun and Moon are represented with the green color, while the black color is used for the model that includes the attraction of Sun and Moon. The initial epoch is J2000 (January 1, 2000, 12:00 GMT).

at an altitude h:

$$\rho(h) = \frac{\rho_{max}(h) + \rho_{min}(h)}{2} + \frac{\rho_{max}(h) - \rho_{min}(h)}{2} \cos\left(\frac{2\pi t}{T} - \phi_0\right), \qquad (6.1)$$

where $\rho_{max}(h)$ and $\rho_{min}(h)$ are computed by using the relation (4.3), T is the period of the solar cycle equal to 11 years, t is the time and ϕ_0 is the phase angle. For instance, in the left panel of Figure 8 we represent the variation of the density ρ at the altitude of $h = 800$ km, between the years 2000 and 2025. The solar activity depends on many factors and, of course, one could refine or propose other equations to model the variation of the density ρ. However, since our aim is to validate the analytical results presented in the previous Section, we shall keep the formulation as simple as possible.

Beside the influence of the solar cycle, we also take into account the lunisolar perturbations. In this case, the conservative part is described by the Hamiltonian

$$\mathcal{K} = \mathcal{H} - \mathcal{R}_{Sun} - \mathcal{R}_{Moon} \ ,$$

where $\mathcal{H}$ is the geopotential Hamiltonian (2.2), while $\mathcal{R}_{Sun}$ and $\mathcal{R}_{Moon}$ are the solar and lunar disturbing functions. We express these functions in terms of the orbital elements of both the perturbed and perturbing bodies by considering the Kaula's expansion of the solar disturbing function (see Kaula (1962)), and the Lane's expansion of the lunar
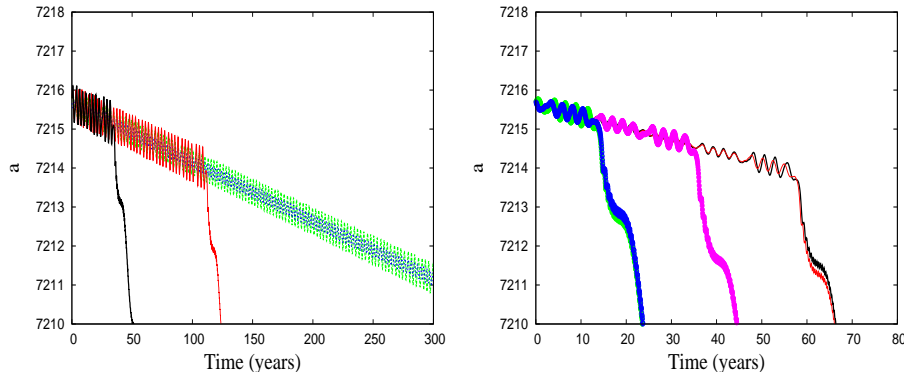
FIGURE 9. Integration of several orbits showing the behavior of the semi-major axis inside the 14:1 resonance, for $B = 100$ $[cm^2/kg]$ (left) and $B = 200$ $[cm^2/kg]$ (right). The initial conditions, at the initial Epoch J2000 (January 1, 2000, 12:00 GMT), are $a = 7215.7$ km, $e = 0.005$, $i = 60^o$, $\omega = 0^o$ and $\Omega = 0^o$, while for the resonant angle we used the following values. Left: $\sigma_{14\,1} = 50^0$ (blue), $\sigma_{14\,1} = 110^0$ (green), $\sigma_{14\,1} = 130^0$ (red), $\sigma_{14\,1} = 150^0$ (black). Right: $\sigma_{14\,1} = 70^0$ (blue), $\sigma_{14\,1} = 80^0$ (black), $\sigma_{14\,1} = 90^0$ (red), $\sigma_{14\,1} = 100^0$ (purple), $\sigma_{14\,1} = 110^0$ (green).

disturbing function (see Lane (1989); Celletti et al. (2017a)). More precisely, the coefficients of R_{Sun}, R_{Moon} expanded in Fourier series are functions of $(a/a_b)^n$, e, e_b, i, and i_b, while the trigonometric arguments are linear combinations of M, M_b, ω, ω_b, Ω, Ω_b, where $n \in \mathbb{N}$, $n \geq 2$ and a_b, e_b, i_b, M_b, ω_b and Ω_b are the orbital elements of the third body (Sun or Moon). Since in computations we deal with finite expressions, we truncate the series expansions of the solar and lunar disturbing functions to a given order in the ratio of the semi-major axes, and moreover we average over the fast angles.

As pointed out in various studies investigating the dynamics in the MEO region (see, e.g., Celletti & Galeş (2016); Celletti et al. (2016); Daquin et al. (2016); Celletti et al. (2017a); Gkolias (2016)), a reliable model is obtained by truncating the expansions to second order in the ratio of the semi-major axes and averaging over both mean anomalies of the point mass and of the third body. Because LEO is closer to the Earth than MEO, then the ratio a/a_b is smaller. Therefore, in LEO the lunisolar perturbations are smaller in magnitude than in MEO. In view of this argument, we shall truncate the series expansions to second order in the ratio of the semi-major axes.
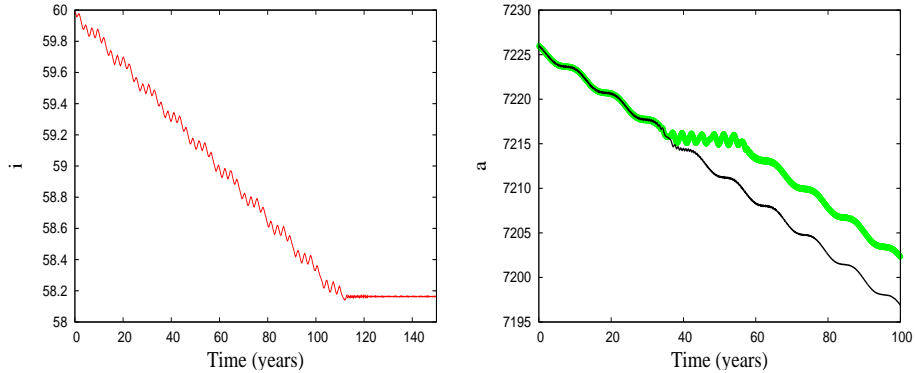
FIGURE 10. Left: behavior of the inclination inside the 14:1 resonance, for $B = 100 \ [cm^2/kg]$, $a = 7215.7 \ km$, $e = 0.005$, $i = 60^o$, $\omega = 0^o$, $\Omega = 0^o$ and $\sigma_{14\,1} = 130^0$. For this orbit, the variation of the semi-major axis is represented in red color in the left panel of Figure 9.
Right: passage through the 14:1 resonance and temporary capture into the 14:1 resonance. The plot is obtained for $B = 100 \ [cm^2/kg]$, $a = 7226 \ km$, $e = 0.005$, $i = 60^o$, $\omega = 0^o$, $\Omega = 0^o$ and $\sigma_{14\,1} = 2^0$ for the black line (passage) and, respectively, $\sigma_{14\,1} = 1^0$ for the green line (capture). The initial epoch for all orbits is J2000 (January 1, 2000, 12:00 GMT).

On the other hand, since in LEO the angles ω and Ω are much faster than in MEO, some resonances of the type (see Celletti et al. (2017b) for further details)

$$\alpha\dot{\omega} + \beta\dot{\Omega} + \alpha_b\dot{\omega}_b + \beta_b\dot{\Omega}_b - \gamma\dot{M}_b = 0 \,, \quad \alpha\,,\alpha_b \in \{\pm 2, 0\}\,, \quad \beta, \beta_b \in \{\pm 2, \pm 1, 0\}\,, \quad \gamma \in \mathbb{Z}\backslash\{0\}\,,$$

where the suffix is $b = S$ when the third-body perturber is the Sun and it is $b = M$ for the Moon, called *(lunar or solar) semi-secular resonances*, might influence the long–term evolution of the orbital elements. For small eccentricities and inclinations between 40 and 120 degrees, an analysis similar to that presented in Celletti et al. (2017b) shows that lunar semi-secular resonances occur at an altitude below 600 km, while solar semi-secular resonances could occur at any altitude in LEO. For this reason, we average the Hamiltonian over the mean anomalies of the satellite and of the Moon, but not over the mean anomaly of the Sun. In this way, we take into account the influence of some possible solar semi-secular resonances. We refer the reader to Celletti et al. (2017a) for the explicit expansions of the disturbing functions $\mathcal{R}_{Sun}$ and $\mathcal{R}_{Moon}$.

The numerical tests done so far show that lunisolar perturbations have a relatively small influence on the long-term evolution of the semi-major axis. In the majority of the cases, we have basically obtained the same behavior of the semi-major axis, either we

have used the full model described above or we have integrated a model that disregards the lunisolar perturbations. However, there are some cases that show a remarkable difference. More precisely, as noticed in Section 5, Figure 4, an orbit reaching the resonant region either it passes through resonance or it is temporarily captured into resonance. This behavior has a strong stochastic feature. Indeed, a small perturbation might lead to a different scenario than expected. For instance, in Figure 8 (right panel), we describe the evolution of the semi-major axis of an orbit, both under the model that disregards the lunisolar perturbations (green line) as well as under the full model that considers the attraction of Moon and Sun (black line). In the first case one gets the phenomenon of temporary capture into resonance, and in the second case the phenomenon of passage through the resonance. For other initial conditions the scenario could be opposite. Therefore, even if the lunisolar perturbations are small in magnitude, they could be important in some cases, as the right panel of Figure 8 shows. The study of lunisolar perturbations and of semi-secular resonances will be a subject of future work.

In Figure 9 we report some results obtained by propagating several initial conditions for a large time, starting from January 1.5, 2000 (J2000). All these initial data are located inside the libration regions of the 14:1 resonance or, to be precise, in the basins of repulsion of the spiral equilibrium points. As the stability analysis presented in Section 5.3 shows, the equilibria of the dissipative toy model (5.9) are repellors. From results of dynamical systems theory, the initial conditions located in the neighborhood of these points do not evolve toward but rather away from them. Thus, within the framework of the dissipative system, the libration regions of the conservative system should become sort of *basins of repulsion*. However, this effect is very small even on long time scales. We will still use the terminology *libration regions*, even in the dissipative case, and not *basins of repulsion* as we should normally adopt in the framework of dissipative dynamical systems.

An important aspect, which enhances the complexity of the dynamics, is the variation of both the position of the equilibrium points, as well as the position and width of the resonant regions, as effect of the solar cycle. Indeed, we find that inside the libration region the initial conditions evolve (slowly) away from the spiral points, as effect of the dissipation. Furthermore, the position of the equilibrium points, and as a consequence the position and width of the libration regions, fluctuates with an 11-year cycle along the $\sigma_{14\,1}$ axis. The amplitude of this variation depends on the value of the ballistic coefficient.

Figure 9 is described better if the results are corroborated with the analytical study presented in Section 5. In particular, the right panel of Figure 7 is relevant for our discussion, since it provides the shift of the equilibria on the $\sigma_{14\,1}$ axis during a solar cycle. Thus, from Figure 7 it follows that for $B = 100 \; cm^2/kg$, the position of the spiral point oscillates between 47° and 75°, while for $B = 200 \; cm^2/kg$ between 50° and 120°. In the left panel of Figure 9, obtained for $B = 100 \; cm^2/kg$, we integrate four orbits, characterized by the same initial conditions with the exception of the resonant angle $\sigma_{14\,1}$ for which we took the following initial values: 50° (blue), 110° (green), 130° (red) and 150° (black). Being sufficiently close to the spiral point, the first two initial conditions lead to *trapped motions* for more than 300 years. Increasing the distance from the spiral point, one obtains *escape motions* with increasingly smaller escape times.

For $i = 60^o$, $e = 0.005$ and ballistic coefficients larger than $200 \; cm^2/kg$, the right panel of Figure 7 shows that equilibrium points do not exist when the solar activity attains its maximum. Thus, for $B = 200 \; cm^2/kg$, we do not expect to obtain trapped motions for hundreds of years. Indeed, the right panel of Figure 9 shows only *escape motions*, but even so, the escape time is very long in some cases. It seems that the longest escape time is obtained for initial values of the resonant angle between 80° (black line) and 90° (red line), namely at the middle of the interval $[50^o, 120^o]$, which represents the range of variation of the position of the spiral point.

Another aspect to be noted is the fact that none of the curves drawn in Figure 9 is horizontal, but rather the semi-major axis slowly decreases in time for each orbit trapped into resonance. For example, in the left plot of Figure 9, the semi-major axis for the orbits represented by blue and green lines decreases of about $4.5 \; km$ within 300 years. This is due to the resonance, which slowly decreases the inclination. Indeed, the left plot of Figure 10 shows the evolution of the inclination for the same orbit for which the variation of the semi-major axis is represented in red color in the left panel of Figure 9. For the trapped motion inside the resonance we notice a slow decrease of inclination from 60° to 58.2^o within about 100 years. Then, after the escape from the resonance, the inclination becomes nearly constant. Since the position of the equilibrium points on the semi-major axis depends on the inclination, see Figure 5 and in particular the bottom right plot of Figure 5 for the 14:1 resonance, a slow decrease of the inclination leads to a shift of the position of equilibrium points along the semi-major axis.

Finally, the right panel of Figure 10 underlines again the stochastic behavior of the orbits reaching the resonant region. We propagate two orbits, whose initial angle $\sigma_{14\,1}$

differs by only one degree. One orbit passes through the resonance and the other is captured temporarily into the resonance. At the light of the results presented in this work, we believe that it would be interesting to study passage or escape from resonances in specific case studies as well as to move parameters or initial conditions to foster one of the two situations, whose exploitation could be conveniently used to design disposal orbits.

References

E. M. Alessi, F. Deleflie, A.J. Rosengren, A. Rossi, G.B. Valsecchi, J. Daquin, K. Merz (2016), *A numerical investigation on the eccentricity growth of GNSS disposal orbits,* Celest. Mech. Dyn. Astr. **125**, n. 1, 71–90.

A. Bezdek, D. Vokrouhlický (2004), *Semianalytic theory of motion for close-Earth spherical satellites including drag and gravitational perturbation,* Planetary and Space Science **52**, n. 14, 1233–1249.

A. Celletti (2010), *Stability and Chaos in Celestial Mechanics,* Springer-Verlag, Berlin; published in association with Praxis Publishing Ltd. (Chichester, ISBN: 978-3-540-85145-5).

A. Celletti, C. Galeş (2014), *On the dynamics of space debris: 1:1 and 2:1 resonances,* J. Nonlinear Science **24**, n. 6, 1231–1262.

A. Celletti, C. Galeş (2015a), *Dynamical investigation of minor resonances for space debris,* Celest. Mech. Dyn. Astr. **123**, 203–222.

A. Celletti, C. Galeş (2015b), *A study of the main resonances outside the geostationary ring,* Advan. Space Res. **56**, 388–405.

A. Celletti, C. Galeş (2016), *A study of the lunisolar secular resonance* $2\dot{\Omega} + \dot{\omega} = 0$, Frontiers in Astronomy and Space Sciences, **3**, 11 pages.

A. Celletti, C. Galeş, G. Pucacco (2016), *Bifurcation of lunisolar secular resonances for space debris orbits,* SIAM J. Appl. Dyn. Syst. **15**, 1352–1383.

A. Celletti, C. Galeş, G. Pucacco, A. Rosengren (2017a), *Analytical development of the lunisolar disturbing function and the critical inclination secular resonance,* Celest. Mech. Dyn. Astr. **127**, n.3, 259–283.

A. Celletti, C. Efthymiopoulos, F. Gachet, C. Galeş, G. Pucacco (2017b), *Dynamical models and the onset of chaos in space debris,* Int. J. Nonlinear Mechanics **90**, 147–163.

C.C. Chao (2005), *Applied Orbit Perturbation and Maintenance,* Aerospace Press Series, AIAA (Reston, Virgina).

J. Daquin, A.J. Rosengren, E.M. Alessi, F. Deleflie, G.B. Valsecchi, A. Rossi (2016), *The dynamical structure of the MEO region: long-term stability, chaos, and transport,* Celest. Mech. Dyn. Astr. **124**, 335–366.

R. Deienno, D. Merguizo Sanchez, A.F. Bertachini de Almeida Prado, G. Smirnov (2016), *Satellite de-orbiting via controlled solar radiation pressure,* Celest. Mech. Dyn. Astr. **126**, n. 4, 433–459.

F. Delhaise (1991), *Analytical treatment of air drag and earth oblateness effects upon an artificial satellite,* Celest. Mech. Dyn. Astr. **52**, n. 1, 85–103.

Earth Gravitational Model 2008, $http : //earth - info.nga.mil/GandG/wgs84/gravitymod/egm2008/$

T.A. Ely, K.C. Howell (1997), *Dynamics of artificial satellite orbits with tesseral resonances including the effects of luni-solar perturbations,* Dynamics and Stability of Systems **12**, n. 4, 243–269.

J.K.S. Formiga, R. Vilhena de Moraes (2011), *15:1 Resonance effects on the orbital motion of artificial satellites,* J. Aerospace Techn Man. **3**, n. 3, 251–258.

C. Froeschlé, E. Lega, R. Gonczi (1997), *Fast Lyapunov indicators. Application to asteroidal motion,* Celest. Mech. Dyn. Astr. **67**, 41–62.

G. Gaias, J.-S. Ardaens, O. Montenbruck (2015), *Model of J_2 perturbed satellite relative motion with time-varying differential drag,* Celest. Mech. Dyn. Astr. **123**, n. 4, 411–433.

G. Gedeon (1969), *Tesseral resonance effects on satellite orbits,* Cel. Mech. **1**, n. 2, 167–189.

I. Gkolias, J. Daquin, F. Gachet, A.J. Rosengren (2016), *From order to chaos in Earth satellite orbits,* Astron. J. **152**, 5.

M. Guzzo, E. Lega, Froeschlé (2002), *On the numerical detection of the effective stability of chaotic motions in quasi-integrable systems,* Physica D. **163**, 1–25.

M. Guzzo, E. Lega (2013), *The numerical detection of the Arnold web and its use for long-term diffusion studies in conservative and weakly dissipative systems,* Chaos **23**, 023124.

A.E. Hedin (1986), *MSIS-86 thermospheric model,* J. Geophys. Res. **92**, 4649–4662.

A.E. Hedin (1991), *Extension of the MSIS thermosphere model into the middle and lower atmosphere,* J. Geophys. Res. **96**, 1159–1172.

ISO 27852:1020(E) (2010), *Space systems – Estimation of orbit lifetime.*

L.G. Jacchia (1971), *Revised static models of the thermosphere and exosphere with empirical temperature profiles,* Smithsonian Astrophysical Observatory, Science Report No. 332, Cambridge, MA.

W. M. Kaula (1962), *Development of the lunar and solar disturbing functions for a close satellite,* Astron. J. **67**, 300–303.

W.M. Kaula (1966), *Theory of Satellite Geodesy,* Blaisdell Publ. Co.

M. T. Lane (1989), *On analytic modeling of lunar perturbations of artificial satellites of the Earth,* Celest. Mech. Dyn. Astr. **46**, 287–305.

W. Larson, J. Wertz (1999), *Space mission analysis and design,* Kluwer publ.

A. Lemaître, N. Delsate, S. Valk (2009), *A web of secondary resonances for large A/m geostationary debris,* Celest. Mech. Dyn. Astr., 104, 383–402.

J.J.F. Liu and R.L. Alford (1980), *Semianalytic theory for a close–Earth artificial satellite,* J. Guidance and Control **3**, n. 4, 304–311.

O. Montenbruck, E. Gill (2000), *Satellite orbits,* Springer.

A.J. Rosengren, D.J. Scheeres (2013), *Long-term dynamics of high area-to-mass ratio objects in high-Earth orbit,* Adv. Space Res. **52**, 1545–1560.

A.J. Rosengren, D.J. Scheeres, J.W. McMahon (2014), *The classical Laplace plane as a stable disposal orbit for geostationary satellites,* Adv. Space Res. **53**, Issue 8, 1219–1228.

A. Roy (2004), *Orbital motion,* (Fourth Edition) Taylor & Francis.

S. Valk, N. Delsate, A. Lemaître, T. Carletti (2009), *Global dynamics of high area-to-mass ratios geosynchronous space debris by means of the MEGNO indicator,* Advances in Space Research **43**, 1509–1526.

Department of Mathematics, University of Rome Tor Vergata, Via della Ricerca Scientifica 1, 00133 Rome (Italy)
E-mail address: `celletti@mat.uniroma2.it`

Department of Mathematics, Al. I. Cuza University, Bd. Carol I 11, 700506 Iasi (Romania)
E-mail address: `cgales@uaic.ro`